SPACOMM 2026

The Eighteenth International Conference on Advances in Satellite and Space Communications

ISBN: 978-1-68558-391-0

May 24 - 28, 2026

Venice, Italy

SPACOMM 2026 Editors

Oliver Michler, Technical University Dresden, Germany

SPACOMM 2026

Forward

The Eighteenth International Conference on Advances in Satellite and Space Communications (SPACOMM 2026), held between May 24-28, 2026 in Venice, Italy, continued a series of events attempting to evaluate the state of the art on academia and industry on the satellite, radar, and antennas based communications bringing together scientists and practitioners with challenging issues, achievements, and lessons learnt.

Significant efforts have been allotted to design and deploy global navigation satellite communications systems, Satellite navigation technologies, applications, and services experience still challenges related to signal processing, security, performance, and accuracy. Theories and practices on system-in-package RF design techniques, filters, passive circuits, microwaves, frequency handling, radars, antennas, and radio communications and radio waves propagation have been implemented. Services based on their use are now available, especially those for global positioning and navigation. For example, it is critical to identify the location of targets or the direction of arrival of any signal for civilians or on-purpose applications; smarts antennas and advanced active filters are playing a crucial role. Also progress has been made for transmission strategies; multiantenna systems can be used to increase the transmission speed without need for more bandwidth or power. Special techniques and strategies have been developed and implemented in electronic warfare target location systems.

We welcomed academic, research and industry contributions. The conference had the following tracks:

- Satellite and space communications
- Satellites and nano-satellites
- Satellite/space communications-based applications

We take here the opportunity to warmly thank all the members of the SPACOMM 2026 technical program committee, as well as all the reviewers. The creation of such a high quality conference program would not have been possible without their involvement. We also kindly thank all the authors who dedicated much of their time and effort to contribute to SPACOMM 2026. We truly believe that, thanks to all these efforts, the final conference program consisted of top quality contributions.

We also thank the members of the SPACOMM 2026 organizing committee for their help in handling the logistics and for their work that made this professional meeting a success.

We hope that SPACOMM 2026 was a successful international forum for the exchange of ideas and results between academia and industry and to promote further progress in the domain of satellites and space communications. We also hope that Venice provided a pleasant environment during the conference and everyone saved some time to enjoy the historic charm of the city.

SPACOMM 2026 Chairs

SPACOMM Steering Committee
Timothy T. Pham, Jet Propulsion Laboratory - California Institute of Technology, USA
Stelios Papaharalabos, u-blox Athens, Greece
Oliver Michler, Technical University Dresden, Germany

SPACOMM Publicity Chairs

José Miguel Jiménez, Universitat Politecnica de Valencia, Spain
Francisco Javier Díaz Blasco, Universitat Politècnica de València, Spain
Ali Ahmad, Universitat Politècnica de València, Spain
Laura Garcia, Universidad Politécnica de Cartagena, Spain
Sandra Viciano Tudela, Universitat Politecnica de Valencia, Spain

SPACOMM 2026

Committee

SPACOMM Steering Committee

Timothy T. Pham, Jet Propulsion Laboratory - California Institute of Technology, USA
Stelios Papaharalabos, u-blox Athens, Greece
Oliver Michler, Technical University Dresden, Germany

SPACOMM 2026 Publicity Chairs

José Miguel Jiménez, Universitat Politecnica de Valencia, Spain
Francisco Javier Díaz Blasco, Universitat Politècnica de València, Spain
Ali Ahmad, Universitat Politècnica de València, Spain
Laura Garcia, Universidad Politécnica de Cartagena, Spain
Sandra Viciano Tudela, Universitat Politecnica de Valencia, Spain

SPACOMM 2026 Technical Program Committee

Bharath H. Aithal, Indian Institute of Technology Kharagpur, West Bengal, India
Zahir A. Hussein Alsulaimawi, Oregon State University, USA
Michael Atighetchi, Raytheon BBN Technologies, USA
Adrian S. Barb, Penn State University, USA
Peter Baumann, Jacobs University, Germany
Aizaz Chaudhry, Carleton University, Canada
Raed S.M Daraghmah, Palestine Technical University, Palestine
Arun Das, Arizona State University, USA
Yiping Duan, Tsinghua University, China
Nour El Madhoun, Laboratoire Sécurité & Système de l'EPITA (LSE), France
Mohamed A. Elshafey, Military Technical College, Cairo, Egypt
Luiz Carlos Gadelha de Souza, Federal University of ABC, Brazil
Gregory Hellbourg, International Center for Radio Astronomy Research | Curtin University, Western Australia
Sundararaja Sitharama Iyengar, Florida International University, USA
Seifallah Jardak, Bristol Research & Innovation Laboratory - Toshiba, UK
Vladimir Karaev, Institute of Applied Physics of *Russian* Academy of Sciences, Russia
Baris Kazar, Oracle America Inc., USA
Mohamed Khalaf-Allah, Friedrich-Alexander University of Erlangen-Nuremberg, Germany
Adil Hakeem Khan, Nation College of Engineering and Technology, Guna, India
Arash Komaee, Southern Illinois University, Carbondale, USA
Nadia Kortas, NASA - Space Communication and Navigation Program (SCaN), USA
Constantine Kotropoulos, Aristotle University of Thessaloniki, Greece
Pablo Madoery, Universidad Nacional de Córdoba, Argentina
Krešimir Malarić, University of Zagreb, Croatia
Michael P. McGuire, Towson University, USA

Oliver Michler, Technical University Dresden, Germany
Sara Migliorini, Università degli Studi di Verona, Italy
Nelli Mosavi, Johns Hopkins University, USA
Nitin Muchhal, Institute of Information Technology (J.I.I.T) Noida, India
Tathagata Mukherjee, The University of Alabama in Huntsville, USA
David N. Amanor, Intel Corporation, USA
Brian Niehoefer, TÜV Informationstechnik GmbH, Germany
Nele Noels, Ghent University, Belgium
W. David Pan, University of Alabama in Huntsville, USA
Krishna Pande, National Chiao Tung University, Taiwan
Cathryn Peoples, Ulster University, UK
Timothy Pham, Jet Propulsion Laboratory, USA
Ermanno Pietrosemoli, The Abdus Salam International Centre for Theoretical Physics (ICTP), Italy
Alexandru Rusu, National University of Science and Technology POLITEHNICA Bucharest, Romania
Takeyasu Sakai, Electronic Navigation Research Institute - National Institute of Maritime, Port and Aviation Technology, Japan
Anoop Kumar Shukla, Manipal Academy of Higher Education, India
Satyavati Shukla, Guilin University of Technology, China
Gulab Singh, Indian Institute of Technology Bombay, India
Predrag Spasojevic, Rutgers University, USA
Cristian Lucian Stanciu, National University of Science and Technology POLITEHNICA Bucharest, Romania
Salvatore Stramondo, Istituto Nazionale di Geofisica e Vulcanologia, Italy
Robert Sundberg, Spectral Sciences Inc., USA
Lahouaria Tabti, Center of Space Techniques/Algerian Space Agency, Algeria
Yuriy Titchenko, Institute of Applied Physics of the Russian Academy of Sciences, Russia
Tin Vu, Microsoft, USA
Xiao Wang, Boston University, USA
Hong Wei, University of Maryland, USA
Yuhang Zang, Nanyang Technological University, Singapore
Yimin Daniel Zhang, Temple University, USA
Yunfan Gerry Zhang, Independent Researcher, USA
Zenghui Zhang, Shanghai Jiao Tong University, China
Guoqing Zhou, Guilin University of Technology, China

Copyright Information

For your reference, this is the text governing the copyright release for material published by IARIA.

The copyright release is a transfer of publication rights, which allows IARIA and its partners to drive the dissemination of the published material. This allows IARIA to give articles increased visibility via distribution, inclusion in libraries, and arrangements for submission to indexes.

I, the undersigned, declare that the article is original, and that I represent the authors of this article in the copyright release matters. If this work has been done as work-for-hire, I have obtained all necessary clearances to execute a copyright release. I hereby irrevocably transfer exclusive copyright for this material to IARIA. I give IARIA permission or reproduce the work in any media format such as, but not limited to, print, digital, or electronic. I give IARIA permission to distribute the materials without restriction to any institutions or individuals. I give IARIA permission to submit the work for inclusion in article repositories as IARIA sees fit.

I, the undersigned, declare that to the best of my knowledge, the article is does not contain libelous or otherwise unlawful contents or invading the right of privacy or infringing on a proprietary right.

Following the copyright release, any circulated version of the article must bear the copyright notice and any header and footer information that IARIA applies to the published article.

IARIA grants royalty-free permission to the authors to disseminate the work, under the above provisions, for any academic, commercial, or industrial use. IARIA grants royalty-free permission to any individuals or institutions to make the article available electronically, online, or in print.

IARIA acknowledges that rights to any algorithm, process, procedure, apparatus, or articles of manufacture remain with the authors and their employers.

I, the undersigned, understand that IARIA will not be liable, in contract, tort (including, without limitation, negligence), pre-contract or other representations (other than fraudulent misrepresentations) or otherwise in connection with the publication of my work.

Exception to the above is made for work-for-hire performed while employed by the government. In that case, copyright to the material remains with the said government. The rightful owners (authors and government entity) grant unlimited and unrestricted permission to IARIA, IARIA's contractors, and IARIA's partners to further distribute the work.

Table of Contents

Optimizing MSS Architecture for Direct-to-Device Services

Santanu Dutta, Ph.D
ClusterSat Network Technologies, LLC
Vienna, VA 22182, USA
email: santanu@clustersat.com

***Abstract*—Direct to Device (D2D) Mobile Satellite Service (MSS), whereby a smartphone connects directly to a satellite, is the flagship of New Space, attracting billions of dollars of investment. To preserve user experience, D2D imposes demanding requirements for maintaining service continuity. Industry analysts are predicting that, for D2D to become mainstream, cellular user-experience must be preserved even when it is offered from space. It is generally agreed that this means offering at least 4G LTE QoS to each user when backing up terrestrial 5G, using 5MHz of allocated channel bandwidth. This is a high bar for legacy satellite networks for two reasons: (1) typical satellite beams are much larger than terrestrial cells, and (2) legacy satellite systems use traditional beamforming for radio access. ClusterSat has shown that a better architecture for D2D would be a fractionated satellite with multiuser MIMO (MU MIMO) for radio access. This architecture synthesizes a very large antenna aperture (~400 m) using a cluster of small satellites, leading to an unprecedented, user spatial resolution of 250 m. Additionally, MU MIMO dynamically focuses radiated power on users requiring service, while protecting other users by satellite-antenna null steering. This approach maximizes capacity density rather than net capacity – an objective that is better aligned with D2D's mission. Using a numerical example, it is shown that ClusterSat's architecture, using a cluster of 1-2 m aperture satellites, offers greater throughput in cellular coverage holes than an 8 m aperture, state-of-the-art (SoA) Low Earth Orbit (LEO) satellite.**

Keywords-Direct-to-Device mobile satellite communications; fractionated satellites; multiuser MIMO from space.

I. INTRODUCTION

D2D has been a dream since the nineties. The value proposition offered by satellite to cellular was *connectivity insurance in cellular-deployed areas* (filling coverage holes) as well as *coverage of underserved areas*. Satellite hoped to gain a major economy-of-scale benefit from integration into cellular smartphones. However, despite increasing throughput, link margin and other capabilities, Mobile Satellite Operators (MSOs) failed to persuade cellular stakeholders to incorporate satellite connectivity in mass market cellphones. The reasons were (i) cell phone integration was initially attempted mostly by GEO satellites operators, wherein the satellite had a much greater link margin challenge than Low Earth Orbit (LEO) satellites; (ii) the market pull for satellite connectivity appeared lacking because of poor user experience. The main reason for the latter was the link margin gap between mobile satellite services (MSS) and cellular -- the best, extant MSS afforded a 4-10 dB link margin on a line-of-sight (LOS) link, compared to over 20 dB for cellular in a non-line-of-sight (NLOS) link. The robustness of cellular services stems partly from this abundant link margin, which compensates for various losses such as building penetration, urban clutter, multipath fading and user body loss.

In the early 2020s, with further advances in MSS and an awareness among cellular Mobile Network Operators (MNOs) of the high cost of 5G infrastructure, interest in satellite backup was rekindled under the banner of D2D. It attracted unprecedented interest/investment, not just from the MSS industry, as in the past, but also from the MNOs. In the USA today, every major MNO has a *D2D strategy* involving alliance with at least one MSO. At present, the MSO leaders appear to be AST SpaceMobile and Starlink. To increase link margin, D2D aspirants have abandoned GEOs in favor of LEOs at 400 – 700 km altitude. However, **questions still remain whether the desired user experience will be delivered by the new LEOs**.

Section 2 discusses KPIs for D2D services – specifically, why capacity-density, rather than net-capacity, might be more appropriate for D2D. Section 3 proposes a new space architecture that is better suited than classical architectures for delivering the preferred KPI. A numerical example is provided to compare the performances of the present system, ClusterSat, and the SoA LEO system, AST SpaceMobile. Section 4 describes the key features of ClusterSat. Section 5 provides some examples of PHY layer Monte Carlo simulations to demonstrate expected performance. Section 6 discusses conclusions from the presented material and outlines envisioned paths to market for the new technology.

II. KEY PERFORMANCE INDICATORS (KPIS) FOR D2D: *CAPACITY DENSITY IS PRIME*

A satellite-cellular hybrid network has two major purposes – (i) filling holes in existing cellular networks and (ii) providing cellular services in areas lacking terrestrial cellular coverage. For this solution to be acceptable, the handovers in (i) must be *truly seamless*. There appears to be consensus [6] that providing 4G LTE in dead cells would meet the seamlessness requirement from a throughput perspective. In (ii), 4G LTE capacity should be available to all users in the designated coverage area, regardless of

ISBN: 978-1-68558-391-0

location – with beamforming, this means blanketing the entire area with sufficient Power Flux Density (PFD) to provide 4G LTE *everywhere*, regardless of user locations.

Industry analysts believe that preserving user experience is essential for D2D's mass market acceptance [1]. Based on the above, we have posited the following **minimum KPI for D2D**.

> ***Each satellite-backed user must be offered at least 4G LTE QoS****, both in the holes of existing cellular networks and in areas without cellular coverage*.

This requirement positions ***capacity density* as a prime KPI, distinct from *net capacity***. In operational terms, achieving high capacity-density requires selectively deploying high capacity (which requires high PFD) in small sub-areas (250 m diameter for ClusterSat) of a satellite beam, where there are users needing satellite service. This requires narrow PFD peaks *inside* a beam at user locations, which is not possible with traditional satellite beams because they create uniform PFD within a beam's footprint.

Unfortunately, the demand-densities of most MSS applications are geographically non-uniform -- they do not match the uniform PFD inside traditional satellite beams. D2D user demands in both urban and rural areas fit the *non-uniform* description. For example, in urban areas, the dead cells form islands of poor- or no-service inside deployed cellular networks, as shown in Figure 1. In rural areas, as shown in Figure 2, the islands may be larger, some exceeding LEO beam sizes. However, even in this case, satellite users are typically distributed randomly in clusters. An example would be users visiting the national park areas in Figure 2. If such users were distributed more uniformly and with greater density, they might motivate terrestrial cellular deployment. In summary: *uniform demand density within a beam is the exception, rather than the norm*, in MSS applications.

Technically, achieving high capacity-density is challenging for a legacy satellite network for the following reasons. Cellular base stations, by virtue of being close to the ground (tens of meters) and equipped with advanced radio access technologies like Multiple-Input-Multiple-Output (MIMO), can deliver extremely high capacity-density (throughput per square kilometer) to user equipment (UEs). In contrast, traditional LEO satellites operate hundreds of kilometers from the ground and have antenna apertures which are (today) up to 8 m for AST SpaceMoble. Such satellites, using traditional beamforming, have a beam footprint of approximately 15 km and frequency reuse distance (for N=3) of over 20 km. In contrast, a macro-cellular network has a frequency reuse distance of a few kilometers (frequency reuse distance is indicative of the deployed capacity density). **The present capacity density gap between traditional MSS and present cellular networks makes it difficult for traditional MSS to deliver 4G LTE to more than a few active users**. This is illustrated with an example use case in Section C.

III. A BETTER ARCHITECTURE TO DELIVER HIGH CAPACITY-DENSITY: *FRACTIONATED SATELLITE AND MU MIMO*

One- and two-meter satellite antenna apertures are used as examples of FR-1 LEOs in 3GPP's NTN reports [2]. As 3GPP reference examples are based on industry consensus, they represent the *knee* rather than an *extremity* of the satellite cost-complexity curve. Today, D2D contenders are exceeding these apertures by orders of magnitude, as indicated above. In ClusterSat's architecture, 1-2 m is the planned aperture of individual satellites (there is a dependence on the operating frequency). As shown in Section C, nine such satellites, operating as per ClusterSat's architecture, offer greater capacity density than the current (State of the Art) SoA LEO with an 8 m antenna aperture. They are competitive even with Starlink, with an estimated 48 m aperture satellite antenna and 1.6 km diameter beam mfootprint.

An assumption of ClusterSat's architecture is that users needing satellite service will (i) have much lower geographical density than cellular users (averaged over a cellular market area), and (ii) be distributed randomly in the said area. Below, we examine the validity and implications of these assumptions using empirical coverage data from FCC databases.

A. Filling coverage holes in deployed cellular markets

A real-world example is shown in Figure 1, corresponding to San Francisco and Washington D.C.

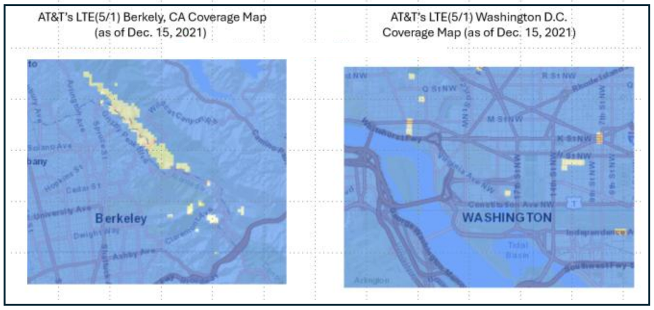

Figure 1. Typical "holes" in urban/suburban cellular coverage

If a regional satellite beam had a diameter of 15 km (like the SoA LEO), much of the downlinked PFD would be wasted because the beam is generally bigger than the coverage hole. In contrast, ClusterSat can focus PFD (and thereby capacity density) on the relatively few UEs in the coverage holes. Note that ClusterSat does not need to cover the entire footprint of regional beam footprint as most of that footprint is covered by the terrestrial cellular network.

B. Providing cellular services in large unserved/underserved areas

A real-world example is shown in Figure 2, corresponding to the Western U.S.A.

In remote areas such as national parks, the beam size *may* be comparable to contiguous areas needing satellite coverage. As these are remote areas, the user density is likely to be low, and the users widely dispersed. As in the case of urban coverage holes discussed above, ClusterSat would have the advantage of dynamically focusing its downlink power on the few users who need service; as the number of users are likely to be small, the number of satellites required would not become huge (the number of satellites is lower bounded by the number of independent hotspots). A traditionally-beamformed single satellite would waste power by radiating it over areas not needing service.

Note: **a traditional satellite can create high capacity-density only if it *also* provides high net-capacity**. This is because its **capacity-density is constant** and its net-capacity is given by net-capacity = (capacity density).(regional beam area). Increasing capacity-density increases net-capacity proportionally. In contrast, **ClusterSat can provide variable capacity-density independently of the net-capacity of its regional beam,** wherein the capacity-density is shaped to match the user density inside the beam**.** To explain further: in the case of ClusterSat, net-capacity = Σ(satellite capacity deployed in each cell inside the beam, or cell-capacity). For ClusterSat, the cell-capacity is non-zero for dead cells and small for live cells, whereas for a traditional satellite, it is constant and high for all cells. The presence of a few dead cells in a beam does not raise the net-capacity to the same level as serving all cells in the beam. **ClusterSat's adaptive capacity-density better optimizes the network relative to its mission, which is to serve dead cells.**

C. Performance comparison: SoA LEO vs. ClusterSat

Figure 3 shows link budget analysis results for a specific use case where the performance of a state-of-the-art (SoA) traditional LEO system (approximately resembling AST SpaceMobile) is compared with ClusterSat for the same usage scenario.

The RF characteristics of AST SpaceMobile were obtained from [7]. The throughputs of both systems were calculated from 5MHz-bandwidth LTE link budgets.

C.1 Scenario assumptions

- User distribution
    - 10 users, non-uniformly distributed in a 15 km diameter circle
- SoA LEO
    - Frequency 2000 MHz
    - Allocated spectrum 5 MHz
    - Tx power in allocated spectrum 11 dBW
    - Altitude 720 km
    - Satellite antenna gain: 41 dBi (corresponds to 8 m aperture)
    - Radio access: Beamforming with 8 m antenna
- ClusterSat
    - Frequency 800 MHz (scalable to any frequency in 800 – 3000 MHz band)
    - Allocated spectrum 5 MHz
    - Tx power in allocated spectrum 4 dBW
    - Altitude 600 km
    - Gain of each satellite antenna: 22 dBi (corresponds to 2 m aperture at 800 MHz)
    - Radio access: MU MIMO with 9 satellites

C.2 Discussion of results

In the scenario shown in Figure 3 both SoA LEO and ClusterSat have identical throughputs (13/3 Mbps, DL/UL) for a single active user. **With 10 active users in the beam, the per-user throughput dilutes to (1.3/0.3 Mbps) for SoA LEO** as, unlike ClusterSat, it lacks the benefit of SDM**. For ClusterSat, thanks to MIMO/SDM, the throughputs can be peaked to their maximum values (13/3 Mbps) individually for each UE** (provided the UEs are more than 250 m apart; otherwise, the throughput is shared by UEs inside a 250 m diameter hotspot).

When compared on the basis of aggregate throughput in a regional beam, SoA LEO shows a net beam-throughput of (13/3 Mbps), while ClusterSat, with 9 satellites, can support up to 7 hotspots, resulting in an aggregate beam-throughput of (91/21 Mbps) -- a **7x net throughput advantage**.

IV. CLUSTERSAT'S ARCHITECTURE

ClusterSat creates small hotspots (250 m diameter) on UEs scheduled to be serviced during a RAN Scheduler scheduled time-frequency block while protecting other, own-network UEs using the same time-frequency block by means of antenna null steering.

The network architecture is shown in Figure 4. The system comprises a primary satellite surrounded by a cluster of smaller ancillary satellites. The number of reuses of an allocated channel scales with the number of satellites. Simulations show that, with 9 satellites, at least 7 users can reuse an allocated channel at a spatial separation greater than 250 m with greater than 10 dB output signal-to-noise-and-interference-ratio (SNIR).

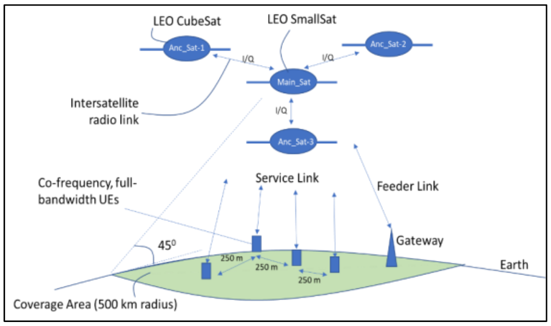

Figure 4. ClusterSat System Architecture

The cluster of satellites flying in formation creates a large-baseline, adaptive, phased array antenna. Each satellite acts as an element of the array, transmitting and receiving signals that are tightly synchronized and processed coherently to synthesize a highly directional, high-capacity communications channel.

The main satellite (Main_Sat) may be a small LEO satellite at 600 km altitude, surrounded by a cluster of ancillary smaller satellites. Size and cost reduction of the Ancillary satellites is possible by allocating most of the digital processing to the Main satellite. The digital processing includes digital-hybrid-beamforming (a combination of MIMO, and traditional, regional beamforming), as well as the typical processing performed by a 3GPP base station onboard a regenerative satellite. Centralizing the bulk of digital processing in the Main satellite has the potential to reduce the role of the Ancillary satellites to remote antennas/transceivers, hence having lower size/weight/power (SWAP). Some similarity with the Remote Radio Head (RRH) functions in Open Radio Access Network (ORAN) architectures may be noted but it should also be noted that all satellites need to be synchronized in their transmit and receive functions, unlike in ORAN. The satellite spacing is approximately 100 m (scaling with frequency). The number of satellites depends on deployment scale (a few to hundreds). The operating frequency will typically be below 3 GHz.

Figure 5 shows an example-configuration of 9 ClusterSat satellites. The cluster comprises a three-dimensional, flexible polyhedron in space. The larger the volume of the polyhedron, the greater the UE spatial resolution is, because a larger polyhedron creates a larger array aperture. In addition to a large array aperture in the x-y plane, the polyhedron also has a reasonable component in the z-direction, radial to the Earth, providing greater angular resolution at lower elevation angles. The satellite cluster will operate in a selected Low Earth Orbit (LEO), but the specific orbital parameters are not critical to the underlying ClusterSat architecture.

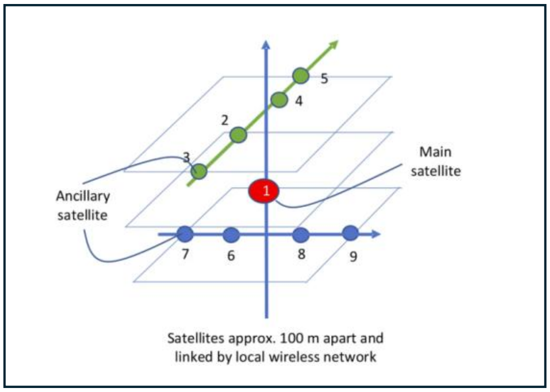

Figure 5. An example of ClusterSat's cluster configuration

The system's core concepts are orbit-agnostic and broadly applicable across a wide range of LEO constellation configurations. As the satellite cluster moves over the face of the Earth, UEs are handed over between different clusters using techniques standardized in 3GPP NTN. It is not necessary that the satellite separations within the cluster be identical or remain strictly constant. In fact, a non-uniform distribution makes the array more robust against grating lobes, which are also avoided by the motion of the cluster in its orbit at 7.5 km/s. The minimum supportable separation between UEs depends on the aperture of the satellite cluster and the system design.

The air interface simulations were performed using a proprietary, OFDM waveform. The latter was similar, but not identical to, 3GPP's MIMO waveform. A simpler (more expedient) waveform than 3GPP was used as the objective of the simulations was to demonstrate the art of the possible, not to emulate the performance with a specific air interface. It is recognized that, for reasons of scale, it may be desirable to leverage 3GPP's MIMO waveforms, although the present, proprietary waveform has performance advantages over 3GPP as it is optimized for a near-LOS satellite channel whereas 3GPP's waveform is designed for a non-LOS cellular channel.

The weight adaptation, based on LMSE optimization, is trained by known pilot signals in both the downlink (DL) and uplink (UL). For the service DL, the complex signals to be transmitted by all satellites, main and ancillary, are created by Main_Sat. The complex baseband (I/Q) signal for each ancillary satellite is communicated to that satellite by the main satellite, together with a GPS time stamp (GPST), over an intersatellite radio link. The GPST indicates the scheduled time of DL transmission, selected by a RAN Scheduler in the main satellite. The DL signals are transmitted by all satellites at the scheduled GPST. **This process ensures that signals transmitted from all satellite antennas are GPS time-synchronized and therefore coherent**. For the service UL, the signal flow is reversed relative to DL. UL signals received by the individual satellites (Ancillary and Main) are down-converted to complex baseband and sent to the Main satellite for processing over the ISL (inter-satellite link). Blocks of signal packet data are accompanied by GPST data (a 100 ms signal block is bound to synchronously sampled GPS UTC data), indicating the time of arrival of the signal data block at the receiving satellite antenna. At the Main satellite, the signals received from the ancillary satellites and the Main satellite are time-aligned and subjected to synthetic beamforming.

V. SIMULATION RESULTS

A large volume of PHY layer Monte Carlo simulations has been performed using representative received SNR. Some sample results are presented in Figure 6. The baseline scenario involves a case of close UE spacings, i.e., 9 UEs were clustered within a 1 km diameter circle, with inter-UE

ISBN: 978-1-68558-391-0

spacings (within the cluster) between 250 m and 1000 m. The simulations involved full-orbit runs, which start from the overhead case of 0^0 nadir angle and end at the nadir angle of 60^0, corresponding to an elevation angle of 18.6^0. Each run involved 135 s of real time operation. The key performance indicators (KPIs) considered were (SNIR) and signal-to-interference-ratio (SIR). SNIR is the prime KPI of the present system as it determines the BER (bit error rate) of digital modulations. The simulated system operated with an input SNR at each satellite of approximately 14 dB. The presented SNIRs show the net result of ClusterSat's MIMO processing on the end-end communications performance. In contrast, the SIR shows how well null steering towards interference sources (a key technology of MIMO) performed. SIR may not always correlate directly with the SNIR, e.g. when the input noise is dominant. For simulations, which involve exclusively the pilot signals, the signal bandwidth is the 15 kHz (bandwidth of one OFDM subcarrier). The results are shown in Figure 6 and the observations are summarized below:

- **SIR reaches high values in all cases** (more than 20 dB when the number of UEs is 4 or more). Even in the theoretically maximum case of 9 UEs, the SIR is above 15 dB for elevation angles above 45° and above 10 dB for elevation angles above 30°. When fewer UEs (e.g. 4) are involved, the SIR is above 20 dB. The high values of SIR indicate that SDM is working – cochannel, simultaneous signals from multiple UEs are experiencing mutual isolations more than 20 dB. The SIR is useful in investigating causes for poor SNIR.
- SNIR shows **no loss over the input SNR of 14 dB in all cases of interest** (elevation angles of 45° or greater). At a 30° elevation angle, insertion loss of from the MIMO process is limited to 3- 4 dB. It should be noted that the "insertion loss" is not really an *operational loss* as it is enabling full-bandwidth channel sharing among all UEs.
- The **SNIR is relatively constant in the region of interest** – elevation angles from 90° to 45°. Most of the SNIR drop occurs between 45° and 30°. This is corelated with the SIR, which also begins to drop in this range; this is expected because the angular resolution required to discriminate between two given UEs increases with decreasing elevation angles.

A. Observations re: simulation results

ClusterSat's system can enable at **least 7-fold frequency reuse** (7 co-frequency, simultaneously transmitting UEs) with **separations on the ground between 250 m.** The degradation beyond 7 UEs is graceful, even while preserving full bandwidth channel sharing. The above spatial frequency reuse is unprecedented for MSS. Altogether, simulations strongly support the core innovations underpinning ClusterSat's concept of operations, comprising:

- Robust MU-MIMO performance using a large-aperture, phased array antenna synthesized from a fractionated satellite cluster, demonstrating no adverse effects from grating lobes, despite longstanding concerns associated with wide spatial baselines.
- Accurate forward-prediction of channel coefficients over time – a patented ClusterSat innovation enabling significant gains in spectral efficiency and reducing reliance on real-time channel estimations.

VI. CONCLUSIONS AND FUTURE WORK

All legacy MSS architectures involve monolithic satellites and traditional beamforming. ClusterSat has shown via simulations/analyses that, except Starlink, present monolithic satellite architectures may be suboptimal in providing D2D services.

D2D requires at least 4G LTE Quality of Service (QoS) for backup service, typically represented by (5/1 Mbps Dl/UL) in 5 MHz of channel bandwidth. Link budget analyses show that, with 8 m satellite antenna aperture, it may be challenging to offer the above QoS to more than a few active users. ClusterSat can meet this challenge for 10 active users with 9 satellites.

Starlink, by pushing the satellite antenna aperture to extreme limits (~48m) *may* be able to deliver the objective QoS as a byproduct of providing Primary, MNO-like services, where net capacity is the primary objective. However, the required capitalization is also extreme. If the primary objective is Supplementary Coverage from Space (SCS), as per the FCC mandate [5], ClusterSat's architecture may be more cost effective and power- and spectrum-efficient.

Currently, ClusterSat does not intend to become a Mobile Satellite Operator (MSO). It plans to license its patented technology, which could comprise the lower-PHY layer of an otherwise standardized protocol like 3GPP NTN NR. Potential licensees could be MSOs, terrestrial cellular operators, or base station platform vendors. The licensing could involve a combination of joint development and supplying ASICs encapsulating the company's beamforming IP. The ASIC would interface with a 3GPP-compliant satellite base station via ORAN interfaces.

REFERENCES

[1] Analyses Mason Direct-to-Device Webinar June 24, 2025.

[2] 3GPP TR 38.821 V16.2.0 (2023-03), Solutions for NR to support non-terrestrial networks (NTN), Release 16.

[3] FCC Report and order and further notice of proposed rulemaking, ADOPTED: MARCH 14, 2024, FCC 24-28, Subject matter: Single Network Future: Supplemental Coverage from Space (SCS).

[4] D. Zlatev, "Starlink set to launch 5G carrier service with drastic satellite constellation expansion", Notebookcheck, September 20, 2025, https://share.google/cea6PvqrIe6ZFSpBT.

[5] J. Brookin, "FCC APPROVES Starlink plan for cellular phone service, with some limits" arsTECHNICA, November 11, 2024,

https://arstechnica.com/tech-policy/2024/11/fcc-approves-starlink-plan-for-cellular-phone-service-with-some-limits/.

[6] The Future of Starlink Direct to Cell, Starlink Update, September 8, 2025.

[7] AST&Science LLC Petition for Declaratory Ruling Granting Access to the U.S. Market for a Non-U.S. Market for a Non-U.S.-Licensed Non-Geostationary Orbit Satellite Constellation, Call Sign S3065, IBFS File Nos. SAT-PDR-20200413-00034, SAT-APL 20200727-00088, & File No. SAT-APL-20201028-00126, April 13, 2020.

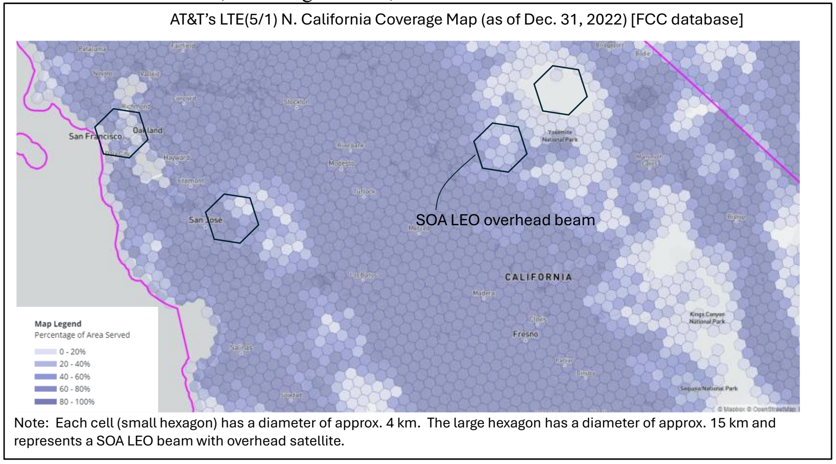

AT&T's LTE(5/1) N. California Coverage Map (as of Dec. 31, 2022) [FCC database]

Note: Each cell (small hexagon) has a diameter of approx. 4 km. The large hexagon has a diameter of approx. 15 km and represents a SOA LEO beam with overhead satellite.

Figure 2. Cellular coverage in remote areas of Western U.S.A.

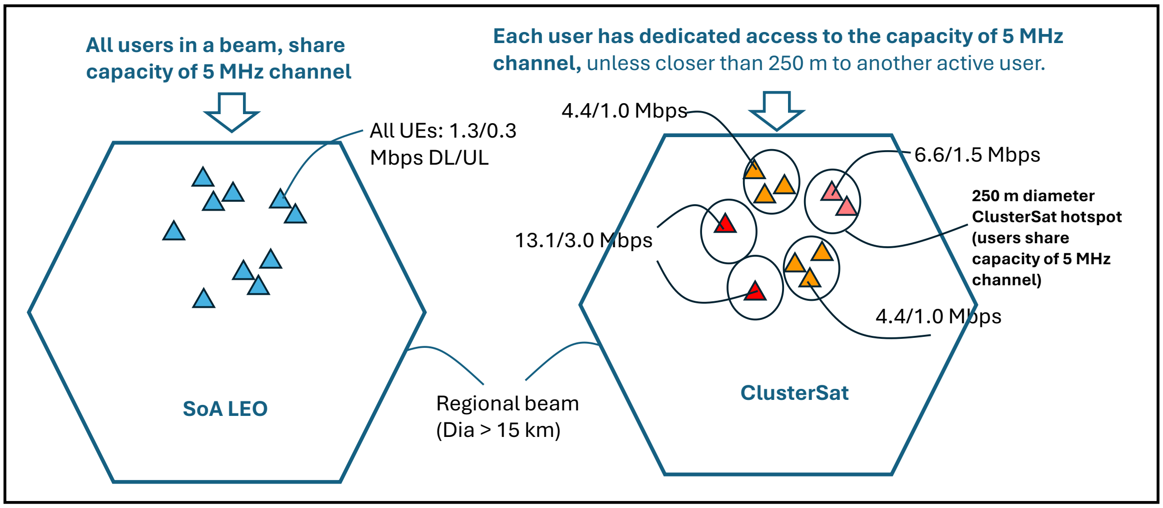

Figure 3. ClusterSat versus legacy SoA LEO

ISBN: 978-1-68558-391-0

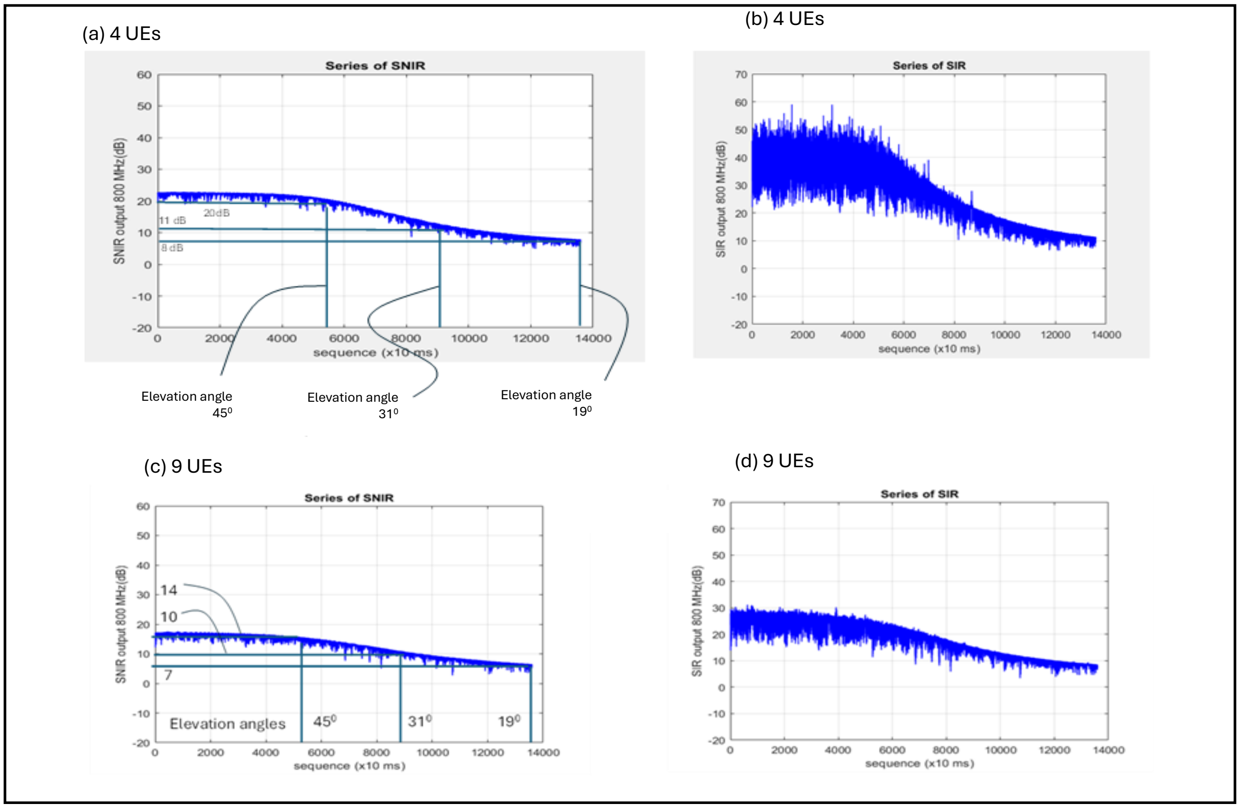

(a) 4 UEs

(b) 4 UEs

(c) 9 UEs

(d) 9 UEs

Figure 6. Simulation results

ISBN: 978-1-68558-391-0

Development of A Registration Technique of Time-series Satellite Image Based on Improved Geometric-matching CNN

Futa Morishima
Department of Mechanical and Control Engineering
Kyushu Institute of Technology
Kitakyushu City, Japan

Tohru Kamiya
Department of Mechanical and Control Engineering
Kyushu Institute of Technology
Kitakyushu City, Japan
Email: kamiya@cntl.kyutech.ac.jp

***Abstract*— One major application of remote sensing data is detecting environmental changes. Image registration, which aligns the coordinates of multiple satellite images acquired over time by different sensors, is an important preprocessing step in this detection process. Conventional registration methods use feature matching to identify features designed by humans, such as Scale-Invariant Feature Transform (SIFT). However, deep learning–based methods for image registration are now being actively studied. While the latest satellite images have a resolution of less than 1 m, processing such high-resolution images can be computationally expensive. Recently, operational systems with Artificial Intelligence (AI) inside satellites have attracted interest. However, the lack of computational resources for onboard computers can also be an issue. In this paper, we propose a lightweight, accurate image registration model with a small number of parameters. Our model is based on geometric matching Convolutional Neural Networks (CNNs) and attempts to reduce the number of parameters by incorporating MobileNetV3, lightweight estimation (LE), and Convolutional Mixers (ConvMixer) to improve registration accuracy. Experimental results on time-series satellite images demonstrate that our method achieves a Grid Mean Squared Error (MSE) of 0.00614, representing the error in image registration. The number of parameters is small. Therefore, the proposed method achieves higher registration accuracy with fewer parameters than the base model.**

Keywords; ConvMixer; Convolutional Neural Network; Geometric-matching CNN; Image Registration, Light-weight Estimation; MobileNetV3; Remote Sensing.

I. INTRODUCTION

In recent decades, the rapid development of satellite and sensor technology has significantly increased the amount of data acquired by remote sensing, resulting in big data [1]. Earth observation satellites are one of the main sources of this data. Figure 1 shows the estimated annual volume of data acquired by three types of Earth observation satellites: Landsat, MODIS, and Sentinel [2]. The volume of data was approximately 0.25 petabytes (PB) in 2013 and exceeded 4.25 PB in 2019. Remote sensing data is used for a wide range of applications. One such application is environmental change detection, a research field that has attracted much attention. This technique uses multiple satellite images taken at the same location to recognize changes in the ground surface. When using multiple satellite images for environmental change detection, it is necessary to compensate for the displacement of the captured area on the image caused by the satellites' attitude. Therefore, image registration, the process of deforming images to overlap the captured areas, is applied as a preprocessing step.

Conventional image registration methods are based on artificial features, such as Scale-Invariant Feature Transform (SIFT) [3] and Accelerated KAZE (AKAZE) [4]. These methods are called "feature-based" and perform registration by detecting and matching feature points to estimate image deformation. Recently, research has focused on satellite image registration methods based on deep learning models. Since these models learn feature representations independently, they are expected to enable more precise image registration than traditional methods, even for satellite images from different time periods and sensors.

However, registering high-resolution satellite images presents a computational cost issue. Generally, the higher the resolution of an image, the higher its registration accuracy [5]. The latest satellites can capture images of the Earth's surface with a resolution of less than 1 meter (m). The use of high-resolution satellite images is increasing. However, processing such images, including registration, is computationally costly due to the large amount of information they contain. Additionally, when considering applications in which an Artificial Intelligence (AI) system is mounted on a satellite's onboard computer, the computer's performance can be problematic. Onboard computers are generally small and lack computing power and memory capacity. This hinders the analysis of large deep learning models.

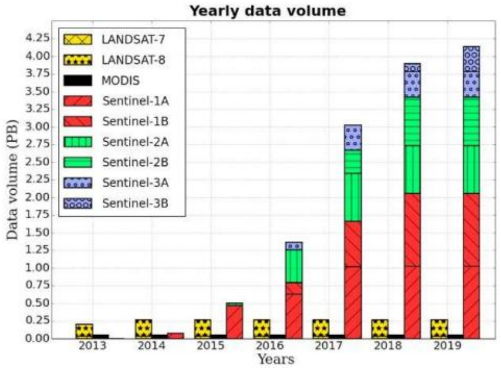

Figure 1. Estimated data volume of satellite images [2].

In this paper, we propose a lightweight, deep learning–based image registration model with a small number of parameters to address the issues. Our method is based on the geometric-matching Convolutional Neural Network (CNN) [6], a CNN-based image registration model that incorporates mechanisms to reduce parameters and improve registration accuracy. We evaluate the accuracy of our proposed method using a time-series satellite image dataset and describe the results.

The rest of this paper is organized as follows: In Section II, we describe our proposed method in detail. Section III presents the experimental results and discussion. Section IV presents the conclusions.

II. METHODS

In this paper, we propose a new registration method for time-series satellite image based on improved geometric-matching CNN approach. The flow of the method is described below.

A. *Geometric-matching CNN*

This paper uses a CNN based on geometric matching as the base model. The model performs registration in three steps: feature extraction, feature matching, and estimation of geometric deformation parameters. During feature extraction, features are extracted from input images I_A and I_B for registration. The input images are normalized. Two backbones with shared weights that are pre-trained by ImageNet extract features from each image. The base model is used up to the middle layer of ResNet101. These features are L2-normalized and used as feature maps, f_A and f_B, in the next step. In the feature matching step, the intermediate output, M_{AB}, is obtained by calculating the inner product of the vectors, f_A and f_B, from the channel directions of each coordinate in the feature maps, f_A and f_B. Then, ReLU (rectified linear unit) and L2 normalization are performed on M_{AB} to produce a similarity map, f_{AB}. Next, the geometric transformation parameter estimation step produces the estimated image transformation parameters, θ_{ES} which are then applied to input images I_A and I_B via the CNN architecture. The network consists of repetitive blocks made up of convolutional layers, Batch Normalization (BN) functions, and Rectified Linear Unit (ReLU) functions. In the base model of this paper, the block containing convolutional layers with 7×7 and 5×5 kernels are repeated twice, respectively. The isotropic affine transformation matrix is output in the final fully connected layer.

B. *MobileNetV3*

The proposed method uses MobileNetV3 [7] as the backbone for feature extraction to reduce the number of model parameters and enable fine-tuning. MobileNetV3 has a structure with multiple bottlenecks in series. Normal convolutional layer operations are divided into pointwise and depthwise convolutions to reduce computational cost. Pointwise convolution uses a 1 × 1 kernel and operates only in the channel direction of the feature map. On the other hand, depthwise convolution uses a single kernel that operates only in the spatial direction of each channel of the feature map. Additionally, a Squeeze-and-Excitation (SE) Layer [8], a type of attention mechanism, is introduced at the bottleneck. The backbone of the proposed model is based on the larger architecture of MobileNetV3, which is more accurate.

C. *Light-weight Estimation*

Lightweight Estimation (LE) has been incorporated into the geometric transformation parameter estimation stage of the network structure of the proposed model. The base model's structure has a significantly higher number of parameters due to convolution on a large, 900-channel feature map. Therefore, LE reduces the number of channels in the similarity map f_{AB} via pointwise convolution. Additionally, an SE layer has been added to improve the balance between parameters and registration accuracy by emphasizing important features.

D. *ConvMixer*

During the geometric transformation parameter estimation step, the ConvMixer model [9] is employed to enhance the precision of image registration. This is accomplished by replacing the base model's block structure with the ConvMixer's. Convolutional layers in CNNs generally have difficulty considering the relevance of information at distant locations in the feature map. ConvMixer overcomes this limitation by using depthwise convolution with a large kernel size to extract information from distant locations. However, depthwise convolution alone cannot extract relevant information in the channel direction. Thus, pointwise convolution is added to learn from the entire feature map. The geometric transformation parameter, θ_{ES} is obtained by applying Global Average Pooling (GAP) and a Fully Connected Layer (FCL) to the output of several consecutive blocks.

E. *Proposed model*

Table I illustrates the structure of the geometric deformation parameter estimation step. Figure 2 illustrates the architecture of the proposed model. As shown in Figure 2, we use MobileNetV3 as the feature extraction network and perform fine-tuning in the feature extraction step to reduce the number of model parameters. In the feature matching step, we incorporate a Cosine Similarity Attention (CSA) module to enhance alignment accuracy. For the following experiments, three comparative models were prepared: the +MNV3 model with MobileNetV3 only, the +LE model with LE applied to the +MNV3 model, and the +CM model with ConvMixer applied to the +MNV3 model. In the +LE model, the number of channels in the geometric deformation parameter estimation step is reduced to 64 while maintaining the same number of parameters as in the proposed model.

III. EXPERIMENTAL RESULTS AND DICUSSIONS

In our experiments, we applied the proposed method to a time series of satellite images. Some of the results and discussions are provided below.

A. *Detail of the dataset*

In our experiment, we apply an isotropic affine transformation to the target image and then register it with the source image. This transformation is randomly selected with a rotation angle between -π/12 and π/12, a scale factor between 0.75 and 1.25, and a translation factor between -0.125 and 0.125. We obtained 2,880 pairs of time-series satellite images from a dataset using Google Earth Pro. The image size is 480X480 pixels. The range of values for the deformation parameters was determined by implementing the geometric matching CNN. Due to the limited number of time-series satellite image pairs, an additional 13,500 images from the PASCAL VOC 2011 dataset [10] are used for training only. This experiment is based on three-fold cross-validation. In each split, the training, validation, and test data consist of 10,500, 420, and 960 image pairs, respectively.

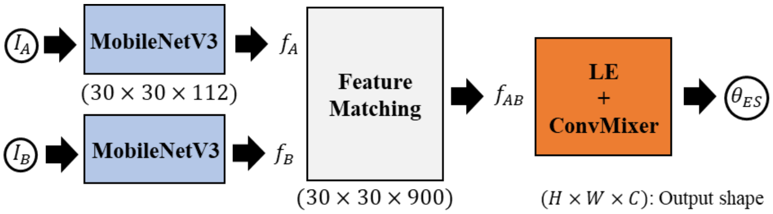

Figure 2 Architecture of proposed model.

TABLE I. STRUCTURE OF PARAMETER ESTIMATION STEOP

(a) BASE MODEL

Layer	Size	Output	Activation
Input f_{AB}	-	30×30×900	-
Conv.1	7×7	24×24×512	BN, ReLU
Conv.2	7×7	18×18×256	BN, ReLU
Conv.3	5×5	14×14×128	BN, ReLU
Conv.4	5×5	10×10×64	BN, ReLU
FCL	-	6	-

(b) PROPOSED MODEL

Layer	Size	Output	Activation
Input f_{AB}	-	30×30×900	-
PwConv.1	1×1	30×30×256	GELU, BN
DwConv.1	9×9	30×30×256	GELU, BN, Res
PwConv.2	1×1	30×30×256	GELU, BN
DwConv.1 ~ PwConv.2 ×2			
SE Layer	-	30×30×256	GELU
DwConv.1 ~ SE Layer ×4			
GAP	-	1×1×256	-
FCL	-	6	-

Pw: Pointwise, Dw: Depthwise, Res: Residual

TABLE II. EXPERIMENTAL RESULTS (EPOCHS=100)

Model	Grid MSE	Params[M]	Throughput [it/s]
Base	0.01579	57.602	15.48
+MNV3	0.01050	30.860	**29.41**
+LE	0.00858	**1.687**	28.46
+CM	0.00645	1.728	27.65
Proposed	**0.00614**	1.760	27.07

B. *Evaluation metrics*

Grid Mean Squared Error (Grid MSE) is used to evaluate the accuracy of image registration. It is also used as a loss function, where a smaller error results in a closer value to zero.

$$MSE_{Grid} = \frac{1}{N}\sum_{i=0}^{N} d((\tau\theta_{ES}(G_i), \tau\theta_{GT}(G_i))^2 \qquad (1)$$

In this experiment, N is set to 400 and represents the number of grid points. G_i is the coordinate of the i-th grid point, and $\tau\theta_{ES}$ and $\tau\theta_{GT}$ represent the change in the coordinate of G_i due to the estimated and ground truth geometric transformation parameters, respectively. We also compare the number of parameters and throughput of the model, as well as registration accuracy.

C. *Results and discussion*

Table II shows the experimental results. The values in the table are the averages from three-fold cross-validation. Compared to the base model, the proposed model has fewer parameters and improves registration accuracy. Figure 3 shows examples of output images from the base and proposed models. The top row shows a target image (the registration target) and a source image (the image used for registration). The second and subsequent rows, from left to right, show the model's output image and the different image. The difference image shows registration errors; red indicates larger deformation than in the target image, and green indicates smaller deformation.

Compared to the base ResNet101 model, MobileNetV3 improves registration accuracy while reducing parameters. This shows that it's possible to improve accuracy while reducing parameters by fine-tuning a dataset suited for the purpose — such as time-series satellite images — rather than just pre-training with ImageNet. Using such a lightweight backbone could be beneficial in situations where computational resources for model training are limited.

In the case of the LE, it is possible to reduce the number of parameters while improving registration accuracy. This is the result of eliminating redundancy in the convolution layer. The SE layer in LE selects important features and reduces redundant parameters through pointwise convolution. This improves accuracy and maintains it. This demonstrates that accuracy can be improved while reducing the number of parameters through pre-training using ImageNet and by fine-tuning the model on purpose-specific datasets, such as time-series satellite imagery. Using such a lightweight backbone is beneficial in situations where computational resources for model training are limited.

The ConvMixer improves registration accuracy without significantly increasing the number of parameters. This improvement stems from depthwise convolution with a nine-kernel size, which has a wide receptive field. This allows the relationship between a pixel and its surrounding regions in the similarity map f_{AB} to be captured. In the ConvMixer block structure, features are extracted while maintaining the feature map's height and width (30×30). Lower-resolution feature maps tend to lose high-frequency feature components, so maintaining the resolution enables registration with more detailed features than the base model.

Due to the modifications described above, the proposed method achieves lower parameters and higher registration accuracy than the base model. However, comparing the throughput of each model shows that reducing parameters does not necessarily lead to faster processing in the execution environment. The +MNV3 model has the fastest throughput; adding LE and ConvMixer decreases processing speed, though it is still faster than the base model. This may be because the implementation in this paper is based on PyTorch, a deep learning framework. Pointwise/depthwise convolutions are computationally less expensive than normal convolutions. Therefore, theoretically, the proposed method should be faster than the +MNV3 model. However, PyTorch optimizes GPU computation for normal convolutions, resulting in faster processing.

Figure 4 shows example images of the alignment results for the proposed method, as well as for image alignment methods based on feature point matching SIFT and AKAZE features. The RANSAC algorithm [12] is applied to the feature point matching method. As can be seen, the proposed method aligns the target image more accurately than the methods using SIFT and AKAZE features, which both produce large errors in image alignment. These errors occur because the correspondence between the detected keypoints is inaccurate, resulting in an incorrect estimated affine transformation matrix. As Figure 4 shows, SIFT and AKAZE features are not robust to time series and color variations among satellite images. However, the proposed method enables the model to learn these differences and perform correct alignment.

Target Source

Map Data: Google, ©2023 Maxar Technologies

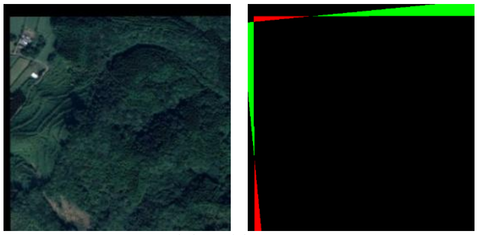

Base model (Grid MSE: 0.00586)

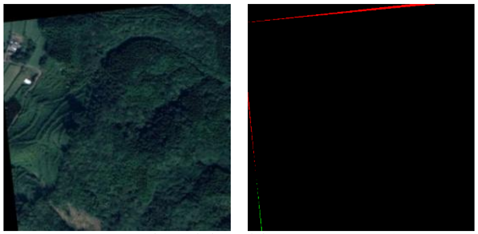

Proposed model (Grid MSE: 0.00017)

Figure 3 Examples of registration results.

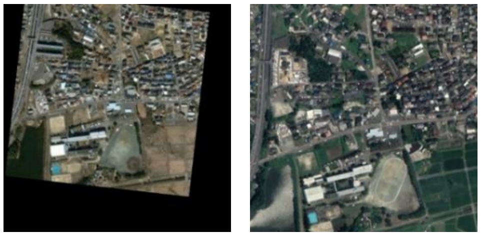

Target Source

Map Data: Google, ©2023 Maxar Technologies

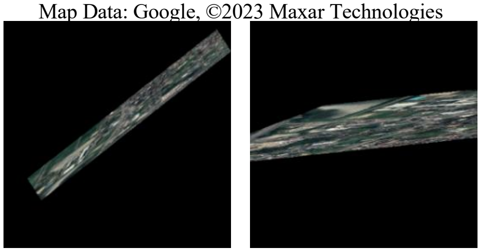

SIFT AKAZE

Ours

Figure 4 A comparison of the proposed method and the feature point matching methods.

IV. CONCLUSION AND FUTURE WORK

This paper was built upon the geometric-matching CNN model, reducing parameters and improving alignment accuracy. In this paper, we propose a method of aligning time series satellite images using deep learning models. The method uses CNN architecture to estimate the geometric transformation parameters necessary for image alignment, taking different time-series satellite images of the present and past as input. We designed the proposed method with a geometrically matching CNN as the base model. We incorporated mechanisms to create a low-parameter model with high positioning accuracy. For instance, we employed the MobileNetV3 backbone structure and LEs to minimize the number of parameters. We also employed the SE Layer and CSA attachment mechanisms. Additionally, we adopted the ConvMixer CNN architecture to improve accuracy while reducing the number of parameters.

Experiments using time-series satellite images were conducted to evaluate the accuracy of the proposed method. Grid MSE, which measures the error in the coordinates of the grid points in the image, and the number of model parameters were used as evaluation indices. The results showed that the proposed method (plus LE and the CM model) performed best with all parameters except CSA. This method reduced Grid MSE by 0.00965 compared to the basic model. Additionally, the number of parameters was smaller than that of the basic model, indicating an improved trade-off between the number of parameters and positioning accuracy in the proposed method.

This experiment evaluates performance based solely on Grid MSE. It is limited in its ability to assess robustness to lighting, seasonal changes, parallax, and scene-specific evaluations. We plan to address these limitations in the future. It will be necessary to further reduce the computational load and improve image alignment accuracy. This will require considering not only the theoretical computational load but also the characteristics of real-world environments, such as those of the PyTorch framework. Additionally, we should consider the practical application of the proposed method to various tasks, such as recognizing environmental changes using time-series satellite images.

ACKNOWLEDGMENT

This paper uses satellite images according to the guidelines of Google Earth [13].

REFERENCES

[1] X. Zhang et al., “Deep Learning for Processing and Analysis of Remote Sensing Big Data: A Technical Review” , Big Earth Data, Vol. 6, No. 4, pp. 527-560, 2022.

[2] P. Soille et al., “A Versatile Data-Intensive Computing Platform for Information Retrieval from Big Geospatial Data” , Future Generation Computer Systems, Vol. 81, pp. 30-40, 2018.

[3] D. G. Lowe, “Distinctive Image Features from Scale-Invariant Keypoints”, International Journal of Computer Vision, Vol. 60, No. 2, pp. 91-110, 2004.

[4] P. F. Alcantarilla et al., “Fast Explicit Diffusion for Accelerated Features in Nonlinear Scale Spaces” , Proc. of British Machine Vision Conference, 2013.

[5] C. Zhao et al., “Effects of Spatial Resolution on Image Registration ” , Proc. of Society of Photo-optical Instrumentation Engineers-the International Society for Optical Engineering, Vol. 9784, pp. 1-16, 2016.

[6] I. Rocco et al., “Convolutional Neural Network Architecture for Geometric Matching” , Proc. of Computer Vision and Pattern Recognition, pp. 6148-6157, 2017.

[7] A. G. Howard et al., “Searching for MobileNetV3” , Proc. of IEEE/CVF International Conference on Computer Vision, pp. 1314-1324, 2019.

[8] J. Hu et al., “Squeeze-and-Excitation Networks” , Proc of IEEE/CVF Conference on Computer Vision and Pattern Recognition, pp. 7132-7141, 2018.

[9] A. Trockman et al., “Patches Are All You Need?” , arXiv preprint arXiv: 2201.09792, 2022.

[10] M. Everingham et al., “The PASCAL Visual Object Classes Challenge 2011 (VOC2011) Results”, http://www.pascal-network.org/challenges/VOC/voc2011/workshop/index.html (Accessed:March/2024)

[11] M. A. Fischler et al., “Random sample consensus: a paradigm for model fitting with applications to image analysis and automated cartography”, Communication of the ACM, Vol.24, No.6, pp.381-395, 1981.

[12] R.Raguram et al., “USAC: A universal framework for random sample consensus”, IEEE Transactions on Pattern Analysis and Machine Intelligence(PAMI), Vol.35, No.8, pp.2022-2038(2013).

[13] Google, “Brand Resource Center”, https://about.google/brand-resource-center/products-and-services/geo-guidelines/ (Accessed:March/2024).

Age of Information in Relativistic Communication Systems

Antonio Franco, Björn Landfeldt
Department of Electrical and Information Technology
Lund University
Lund, Sweden
e-mail: `{antonio.franco, bjorn.landfeldt}@eit.lth.se`

***Abstract*—Age of Information (AoI) is a widely used metric to quantify the freshness of updates in communication systems. Existing AoI analyses implicitly assume a shared or synchronized notion of time between transmitter and receiver, thereby neglecting distortions arising from relative motion and gravitational effects. In this paper, we investigate the impact of relativistic time dilation on information freshness and introduce a relativistic formulation of peak Age of Information (pAoI). We first study a special-relativistic setting in which a transmitter moves at constant velocity relative to a receiver, showing that naive timestamp comparison leads to systematic errors in pAoI evaluation, even at moderate velocities. When transmitter velocity is unknown, we characterize the uncertainty induced by velocity estimation and demonstrate that a polynomial estimator can accurately reconstruct the generation time in the receiver reference frame. We then extend the framework to general relativity using a weak-field approximation that jointly accounts for gravitational and kinematic clock-rate distortions. Leveraging established satellite clock modeling techniques, we show that local polynomial approximation enables effective recovery of information freshness despite unknown relativistic effects. Numerical results validate the proposed estimators across all velocity and orbital regimes. This work establishes a first connection between relativistic time modeling and AoI, providing a foundation for freshness analysis in satellite, deep-space, and high-mobility communication systems relevant to space communications and navigation.**

Keywords-age of information; special relativity; general relativity; GNSS; time dilation.

I. INTRODUCTION

Timely information delivery is a fundamental requirement in modern communication and control systems, where decisions are often made based on the most recently received status updates. In such systems, the notion of freshness captures how well the information available at a receiver reflects the current state of a remote source. The concept of freshness was formalized through the AoI metric, introduced in [1], which measures the time elapsed since the generation of the latest successfully received update. A closely related measure is the pAoI [2], defined as the maximum age immediately prior to the reception of an update. AoI and pAoI have since become central performance metrics in the analysis and design of communication systems (for a comprehensive survey on AoI, see [3][4]).

Most existing AoI analyses implicitly assume a shared or synchronized notion of time between transmitter and receiver, or equivalently neglect distortions arising from relative motion and gravitational effects. This assumption is reasonable for terrestrial networks, but becomes questionable in high-mobility or space-based systems, where relativistic time dilation can significantly affect the interpretation of timestamps.

In contrast to navigation and timing systems, such as Global Navigation Satellite Systems (GNSS), where relativistic effects are corrected using known orbital parameters [5][6], we consider a communication-theoretic setting in which transmitter motion and gravitational effects are not known a priori and must be inferred from received signals or timestamps. In this context, relativistic distortions directly impact the perceived freshness of information. Motivated by established clock modeling practices in satellite timing systems [7], we adopt a receiver-side polynomial correction framework to mitigate relativistic effects on information freshness. This approach enables accurate reconstruction of the pAoI without requiring explicit knowledge of transmitter velocity or gravitational potential. The main contributions of this paper are as follows:

- We introduce a relativistic formulation of pAoI, explicitly accounting for time dilation induced by relative motion and gravity.
- For special relativity, we show that naive timestamp comparison leads to systematic pAoI errors, and we characterize the uncertainty introduced when transmitter velocity is unknown.
- We propose a carrier-free polynomial estimator that reconstructs the generation time in the receiver reference frame using only timestamped updates, and demonstrate that it consistently outperforms the naive method.
- We extend the estimator framework to general relativity using a weak-field approximation, enabling pAoI recovery under combined gravitational and kinematic clock distortions.
- Through numerical simulations, we validate the proposed estimators and quantify their accuracy improvements over naive AoI evaluation.

We emphasize that the estimators introduced in this work are not designed to reduce the pAoI through scheduling, preemption, or control mechanisms. Instead, they address a measurement problem: how pAoI should be consistently estimated at the receiver when the transmitter and receiver experience different proper times due to relativistic effects. The underlying update generation process and service discipline remain unchanged.

The remainder of this paper is organized as follows. In Section II, related work is presented. In Section III, AoI is characterized in the context of Special Relativity and a pAoI estimator is developed. In Section IV, AoI is characterized in

ISBN: 978-1-68558-391-0

the context of General Relativity and another more sophisticated pAoI estimator is developed. In Section V, the previous estimators are compared with simulations and results analyzed. Finally, in Section VI, conclusions and future work are discussed.

II. RELATED WORK

A growing body of work has investigated AoI in satellite and non-terrestrial networks, particularly in Low Earth Orbit (LEO) systems [8]–[16]. These contributions analyze AoI and pAoI under stochastic geometry, queueing, and scheduling perspectives, incorporating practical aspects such as intermittent connectivity, propagation delay, interference, and satellite mobility. However, in these works, Doppler effects are typically treated as impairments affecting signal quality or access probability, while propagation delay is often modeled as a deterministic or slot-based quantity. The relativistic nature of time itself – namely, the fact that timestamps generated onboard a moving or gravitationally displaced transmitter correspond to a different proper time than that of the receiver – is not explicitly modeled. Consequently, the AoI metric is evaluated under the implicit assumption that transmitter timestamps are directly comparable to receiver time.

Relativistic effects have been extensively studied in the context of satellite time and frequency synchronization, most notably within GNSSs. The foundational treatment by Ashby [5] provides a comprehensive analysis of both special and general relativistic effects affecting satellite clocks, including gravitational frequency shifts, time dilation due to orbital motion, the Sagnac effect, and relativity of simultaneity. These effects are sufficiently large that, without explicit correction, accurate positioning and timing would be impossible.

Subsequent works have focused on characterizing and modeling residual clock errors after relativistic correction. In [6], the authors analyze periodic variations in Global Positioning System (GPS) satellite clocks arising from orbital dynamics and relativistic effects, demonstrating that residual clock behavior can be effectively modeled using deterministic components. More recently, polynomial clock prediction models have become standard in precise point positioning and timing applications, where satellite clock offsets are represented using low-order polynomials capturing phase, frequency offset, and frequency drift [7].

Receiver-side clock modeling has also been shown to significantly improve synchronization performance. In [17], the authors demonstrate that treating receiver clock offsets as structured stochastic processes rather than white noise yields substantial gains in timing stability, further reinforcing the importance of deterministic clock modeling in satellite timing systems.

To the best of our knowledge, no existing AoI-centric study explicitly incorporates relativistic time dilation or gravitational frequency shifts into the definition, estimation, or statistical characterization of AoI. In particular, the effect of estimating transmitter velocity or gravitational potential on the uncertainty of AoI has not been addressed. This work bridges this gap by integrating relativistic time modeling with AoI analysis, and by proposing estimators that reconstruct the AoI in the receiver's time frame under both special and general relativity.

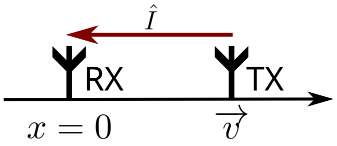

Figure 1. Reference frame for the constant relative speed scenario.

III. SPECIAL RELATIVITY

In this section, we develop the framework to model pAoI in a special-relativistic setting. We first introduce the system model for a transmitter moving at constant velocity along the line of sight to the receiver, and show how relativistic time dilation distorts naive timestamp-based pAoI evaluation. We then address the practical case in which the transmitter velocity is unknown at the receiver, characterizing the resulting estimation uncertainty and proposing a timestamp-only polynomial estimator that recovers the generation time in the receiver reference frame.

A. Model

Consider a transmitter (TX) that sends a piece of information $\hat{I}$ to a receiver (RX), where TX always timestamps $\hat{I}$ with its onboard time at the moment of transmission. The RX is located at the origin of its reference frame, while the TX moves at constant speed v along the x-axis (see Figure 1). We assume that a synchronization event has occurred, meaning that TX and RX met at the same position and set their clocks to 0 at that moment. For simplicity, we assume that the physical dimensions of both TX and RX are negligible and that gravitational effects are absent. We further assume that the transmission length of $\hat{I}$ itself – from header to end of content – is negligible, such that the piece of information along with its timestamp, upon reception, is decoded immediately. The propagation medium is vacuum.

We denote the RX proper time – i.e., the time measured in the frame of reference of RX – with t, and the TX proper time with τ. The TX timestamps $\hat{I}$ with τ_g, as measured by its onboard clock. Due to special-relativistic time dilation, the proper time τ of TX and the coordinate time t in the RX frame are related by:

$$\tau = \frac{t}{\gamma}\,, \tag{1}$$

$$\gamma = \frac{1}{\sqrt{1-\beta^2}}\,, \tag{2}$$

$$\beta = \frac{v}{c}\,,$$

where c is the speed of light in vacuum. When TX timestamps τ_g, the RX frame emission time is:

$$t_g = \gamma\tau_g\,. \tag{3}$$

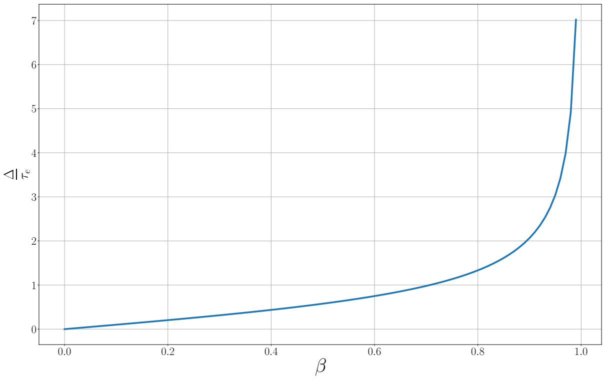

Figure 2. Normalized pAoI at RX vs β.

Since we assume constant speed v, the position of TX at an arbitrary time t is $x(t) = vt$. The update generation position x_g – i.e., the position of TX with respect to RX at the moment of the generation of the update t_g, as measured by the RX onboard clock – is then:

$$x_g = vt_g = v\gamma\tau_g \,. \tag{4}$$

The propagation time is $\frac{x_g}{c}$, and therefore the reception time t_r at RX is:

$$t_r = t_g + \frac{x_g}{c} = \gamma\tau_g + \frac{v\gamma\tau_g}{c} = \gamma(1+\beta)\tau_g \,.$$

Notice that for TX approaching RX (moving toward RX), the sign flips:

$$t_r = \gamma(1-\beta)\tau_g \,.$$

For a more compact representation, we group both multipliers in the Doppler factor:

$$k_\pm = \gamma(1 \pm \beta) = \sqrt{\frac{1 \pm \beta}{1 \mp \beta}} \,, \tag{5}$$

so that

$$t_r = k_\pm \tau_g \,.$$

A naive approach to evaluating the pAoI would be to directly compare the timestamp of $\hat{I}$ with the RX onboard time:

$$\Delta_{\text{naive}} = t_r - \tau_g = \tau_g(k_\pm - 1) \,.$$

However, this yields a negative value for $k_\pm < 1$, which occurs when TX approaches RX. A more correct approach is to calculate the pAoI $\Delta(t_g)$ as:

$$\Delta = t_r - t_g = \frac{|x_g|}{c} = \frac{\gamma|v|\tau_g}{c} = \gamma|\beta|\tau_g \,, \tag{6}$$

where we used (4) to expand x_g. Equation (6) establishes a clear relationship between pAoI and relative speed. In Figure 2, the pAoI, normalized to τ_g, is plotted against β. As shown, the pAoI grows as the speed of TX approaches the speed of light.

Now assume that TX sends updates according to a random process with average rate λ_{TX} updates per second, i.e., with average spacing $\frac{1}{\lambda_{TX}}$. By applying the well-known formula for the relativistic Doppler effect (similar to (1)) the arrival rate as seen by RX is:

$$\lambda_{RX} = \frac{\lambda_{TX}}{\gamma} \,,$$

More generally, let θ denote the angle between the TX velocity and the Line of Sight (LOS) toward RX. Then:

$$\lambda_{RX} = \frac{\lambda_{TX}}{\gamma(1 - \beta\cos(\theta))} \,.$$

This shows that updates arrive faster at the RX when the TX moves toward it (resulting in lower AoI measured onboard the RX), and slower when it moves away (resulting in higher AoI measured onboard the RX). Note that the entire AoI process is affected by the Doppler effect, which can yield long tails in the distribution even when this effect is unintended.

B. *Estimating pAoI*

Until now, we have assumed that the magnitude and direction of the transmitter velocity are known, which allows us to recover the AoI in RX time via (6). We now study how uncertainty in v affects the AoI measured on the RX side.

1) Carrier Frequency Estimation: The simplest method to estimate v is for TX and RX to share knowledge of a carrier frequency f_0. Then RX can simply calculate the difference with the measured frequency $\hat{f}_0$ and from there determine the Doppler factor, and thus t_g in its reference frame via (1). In particular, we assume that TX moves inertially at constant speed along the LOS, that no scattering occurs, and that the physical layer decodes correctly. We ignore symbol deformation and similar effects. In this case, the pAoI at reception time is itself an estimate:

$$\Delta = t_r - \hat{t}_g \,, \tag{7}$$

where $\hat{t}_g$ is RX's estimate of the generation time expressed in the RX time coordinate. Since γ is a function of β (2), we have:

$$\hat{t}_g = \gamma(\hat{\beta})\tau_g \,.$$

We define the conversion-error random variable as:

$$\epsilon = t_g - \hat{t}_g = \gamma(\beta)\tau_g - \gamma(\hat{\beta})\tau_g \,.$$

The mapping $\gamma(\hat{\beta})$ can be approximated by a first-order Taylor expansion around the true β. The first-order approximation is justified under standard asymptotic conditions for Doppler-based estimators, such as sufficiently high Signal-to-Noise Ratio (SNR) or long coherent observation time [18]. Thus:

$$\begin{aligned} \gamma(\hat{\beta}) &= \gamma(\beta) + \gamma'(\beta)\,(\hat{\beta} - \beta) + O\Big((\hat{\beta} - \beta)^2\Big) \\ &\approx \gamma(\beta) + \gamma'(\beta)\,(\hat{\beta} - \beta) \,, \end{aligned}$$

which yields:

$$\epsilon \approx -\tau_g\gamma'(\beta)\,(\hat{\beta} - \beta) \,.$$

Finally, since in (7) the only uncertainty is in the estimated t_g, we can conclude:

$$\mathrm{Var}(\Delta) \approx \mathrm{Var}(\epsilon) = \mathrm{Var}\left(-\tau_g\gamma'(\beta)\,(\hat{\beta} - \beta)\right)$$

$$= \tau_g^2 \gamma'(\beta)^2 \operatorname{Var}(\hat{\beta} - \beta) = \tau_g^2 \beta^2 \gamma(\beta)^3 \operatorname{Var}(\hat{\beta}) \,, \qquad (8)$$

where we used (2) to expand $\gamma'(\beta)$.

It remains to relate $\operatorname{Var}(\hat{\beta})$ to $\operatorname{Var}(\hat{f}_r) = \sigma_f^2$, where $\hat{f}_r$ is the estimate of the Doppler-shifted frequency as seen from RX. By solving (5) for β in terms of $k_\pm$, we obtain:

$$\beta_- = \frac{1 - k_-^2}{1 + k_-^2}$$
$$\beta_+ = -\frac{1 - k_+^2}{1 + k_+^2} \,.$$

We proceed with the case k_-; the derivation for k_+ is analogous and yields the same result. Taking the first derivative with respect to β we get:

$$\gamma'(\beta) = \beta \gamma^3 \,.$$

Using the same logic applied in deriving (8), and noting that the Doppler factor is also the ratio between f_r and f_0, we obtain:

$$\begin{aligned}&\operatorname{Var}(\hat{\beta}) = \operatorname{Var}(\beta(\hat{k}_-)) \approx \operatorname{Var}(\beta(k_-) + \beta'(k_-)(\hat{k}_- - k_-)) \\ &= \beta'(k_-)^2 \operatorname{Var}(\hat{k}_-)\end{aligned}$$

Finally, substituting this result into (8) yields:

$$\operatorname{Var}(\Delta) \approx \tau_g^2 \beta^2 \gamma^6 \frac{16 k_-^2}{(1 + k_-^2)^4} \frac{\sigma_f^2}{f_0^2} \,.$$

Thus, the standard deviation in the estimated pAoI grows proportionally with the uncertainty in the carrier frequency estimate.

2) pAoI Polynomial Estimator: The receiver observes a stream of timestamped updates. Each update carries the transmitter-side generation timestamp $\tau_g^{(n)}$, expressed in the TX proper-time reference frame, and is received at the RX at time $t_r^{(n)}$, measured by the RX onboard clock. While $\tau_g^{(n)}$ is explicitly available in the packet payload, the corresponding generation time expressed in the RX time coordinate, $t_g^{(n)}$, is not directly observable due to relativistic time dilation and propagation effects. As a result, a naive AoI computation based on directly comparing $t_r^{(n)}$ and $\tau_g^{(n)}$ yields incorrect or even unphysical results, as discussed in Section III-A.

The objective of the pAoI polynomial estimator is therefore to reconstruct, at the receiver, an estimate of the generation time expressed in the RX time coordinate, $\hat{t}_g(\tau_g^{(n)})$, using only the sequence of observed timestamp/arrival-time pairs $\{(\tau_g^{(i)}, t_r^{(i)})\}$. Once such an estimate is available, the pAoI at reception can be formed as

$$\hat{\Delta}_n \triangleq t_r^{(n)} - \hat{t}_g(\tau_g^{(n)}),$$

without relying on carrier-based Doppler estimation or prior knowledge of the transmitter velocity.

Polynomial approximation of the time-transfer mapping: Motivated by established clock modeling techniques in high-precision timing systems [7], we approximate the mapping between the TX timestamp τ and the RX reception time t_r locally in time by a low-order polynomial. Over a sufficiently short observation window, we write

$$\hat{t}_r(\tau) = a_0 + a_1 \tau + a_2 \tau^2 + \dots \,, \qquad (9)$$

where the coefficients $\{a_k\}$ capture the combined effects of relativistic time dilation, propagation delay, and any slowly varying mismatch between the TX and RX clocks.

Least-squares coefficient estimation: Given a sliding window of N received updates $\{(\tau_g^{(i)}, t_r^{(i)})\}_{i=n-N+1}^{n}$, the RX estimates the polynomial coefficients by Ordinary Least Squares (OLS). Defining the observation vector $\mathbf{t}_r$ and the Vandermonde design matrix $\mathbf{X}$ as:

$$\mathbf{t}_r \triangleq \begin{bmatrix} t_r^{(n-N+1)} & \cdots & t_r^{(n)} \end{bmatrix}^T ,$$
$$\mathbf{X} \triangleq \begin{bmatrix} 1 & \tau_g^{(n-N+1)} & (\tau_g^{(n-N+1)})^2 & \cdots \\ \vdots & \vdots & \vdots & \\ 1 & \tau_g^{(n)} & (\tau_g^{(n)})^2 & \cdots \end{bmatrix} ,$$

the coefficient estimate is:

$$\hat{\mathbf{a}} = (\mathbf{X}^T \mathbf{X})^{-1} \mathbf{X}^T \mathbf{t}_r \,.$$

The matrix $\mathbf{X}^T \mathbf{X}$ is invertible provided that the RX observes at least $p{+}1$ updates at distinct timestamps over the estimation window, which is naturally satisfied in any non-degenerate AoI process.

From polynomial fit to generation-time estimation: In the constant-velocity, LOS scenario considered in this section, special relativity implies that the reception time is related to the TX timestamp by a Doppler factor $k_\pm$, i.e., $t_r = k_\pm \tau$. Consequently, the Doppler factor can be identified with the derivative of the reception-time mapping with respect to τ. Using the fitted polynomial (9), the RX forms

$$\hat{k}_n \triangleq \frac{d}{d\tau} \hat{t}_r(\tau) \big|_{\tau = \tau_g^{(n)}} .$$

The corresponding velocity and Lorentz factor estimates follow directly from the relativistic Doppler relation, yielding $\hat{\beta}_n$ and $\hat{\gamma}_n$. Finally, the RX estimates the generation time expressed in its own reference frame as

$$\hat{t}_g(\tau_g^{(n)}) = \hat{\gamma}_n \, \tau_g^{(n)} .$$

pAoI estimation procedure: The complete AoI synchronization and estimation procedure is summarized in Figure 3. The algorithm operates purely on timestamped packet arrivals and produces a pAoI estimate at each reception instant once the estimator reaches steady state.

IV. GENERAL RELATIVITY

In contrast to the special-relativistic setting, where the relationship between transmitted timestamps and reception times admits a closed-form expression, the general-relativistic case does not generally yield an explicit mapping, like the one expressed by (3). Relativistic clock-rate differences and propagation effects depend on the gravitational field and on the spacetime geometry encountered along the signal path. As

```
Require: Polynomial degree $p$; window size $N \geq p+1$; stream of received updates $\{(\tau_g^{(n)}, t_r^{(n)})\}$
Ensure: pAoI estimate at reception $\hat{\Delta}_n$ and generation-time estimate $\hat{t}_g(\tau_g^{(n)})$
Maintain a sliding window $\mathcal{W}_n = \{(\tau_g^{(i)}, t_r^{(i)})\}_{i=n-N+1}^{n}$
if $|\mathcal{W}_n| < N$ then
    return (insufficient samples)
Build $\mathbf{X} \in \mathbb{R}^{N\times(p+1)}$ with rows $\left[1,\ \tau_g^{(i)},\ (\tau_g^{(i)})^2,\ \ldots,\ (\tau_g^{(i)})^p\right]$
Stack $\mathbf{t}_r \leftarrow [t_r^{(n-N+1)}, \ldots, t_r^{(n)}]^T$
Compute OLS coefficients $\hat{\mathbf{a}} \leftarrow (\mathbf{X}^T\mathbf{X})^{-1}\mathbf{X}^T\mathbf{t}_r$
Evaluate Doppler-factor estimate via the derivative:
    $\hat{k}_n \leftarrow \frac{d}{d\tau}\hat{t}_r(\tau)\big|_{\tau=\tau_g^{(n)}} = \sum_{m=1}^{p} m\,\hat{a}_m \left(\tau_g^{(n)}\right)^{m-1}$
Invert the SR Doppler relation (LOS case) to obtain
    $\hat{\beta}_n \leftarrow \frac{\hat{k}_n^2 - 1}{\hat{k}_n^2 + 1}, \qquad \hat{\gamma}_n \leftarrow \frac{1}{\sqrt{1-\hat{\beta}_n^2}}$
Compute generation-time estimate in RX coordinates:
    $\hat{t}_g(\tau_g^{(n)}) \leftarrow \hat{\gamma}_n\,\tau_g^{(n)}$
Output pAoI estimate at reception:
    $\hat{\Delta}_n \leftarrow t_r^{(n)} - \hat{t}_g(\tau_g^{(n)})$
```

Figure 3. pAoI Polynomial Synchronization at RX (timestamp-only).

a result, the AoI evaluation problem in the general-relativistic setting naturally leads to an estimator-based formulation, which reconstructs the time-transfer mapping directly from timestamped observations.

A. Model

Consider a TX that sends timestamped updates to an RX, where each update is labeled with the TX onboard clock reading at the moment of generation. Both TX and RX are equipped with ideal clocks measuring their respective proper times. Unlike the special-relativistic case, we now allow the spacetime to be curved due to the presence of a gravitational field. TX and RX follow prescribed worldlines in a weak gravitational field, and their clocks generally tick at different rates due to both relative motion and gravitational time dilation. We assume that a synchronization event has occurred at some initial spacetime point, after which TX and RX clocks are related only through the exchange of timestamped signals. The physical dimensions of TX and RX are assumed negligible, and the transmission duration of each update is assumed small compared to the timescales of interest. Signal propagation occurs through vacuum along null trajectories of the spacetime geometry (a null trajectory is the spacetime path followed by light or radio signals; while such signals always propagate at the speed of light locally, gravity can bend their paths and modify their travel times, an effect accounted for by general relativity).

Let τ denote the TX proper time and t the RX proper time, measured by their respective onboard clocks. Each update generated at TX at time τ_g is received by RX at time t_r. In the presence of gravitational fields, the relationship between τ_g and t_r is governed by relativistic clock-rate differences and by signal propagation along curved spacetime trajectories. These effects jointly induce a deterministic but generally unknown time-transfer mapping between TX timestamps and RX reception times, which we denote by:

$$t_r = \mathcal{T}(\tau_g). \tag{10}$$

Unlike the special-relativistic case, this mapping does not generally admit a closed-form expression and may vary slowly over time due to changes in gravitational potential or non-inertial motion. For reference, the usual weak-field approximation for the rate at which TX proper time τ elapses with respect to RX time t [5] is $\frac{d\tau}{dt} \approx 1 - \frac{\Phi(x)}{c^2} - \frac{v^2}{2c^2}$, where $\Phi(x)$ is the Newtonian gravitational potential at position x and v is the instant relative velocity.

The pAoI at reception is defined with respect to RX time as

$$\Delta = t_r - t_g\,,$$

where t_g denotes the generation time expressed in the RX time coordinate. Since t_g is not directly observable at the receiver, evaluating the AoI in the general-relativistic setting requires estimating the inverse relationship between the transmitted timestamp τ_g and the corresponding generation time in the RX reference frame. This observation motivates the estimator-based approach developed in the following subsection.

B. pAoI Polynomial Estimator

The receiver observes a sequence of timestamped updates, where each update carries the TX proper-time timestamp $\tau_g^{(n)}$ and is received at RX time $t_r^{(n)}$. As established in Section IV-A (10), these quantities are related through an unknown time-transfer mapping $t_r = \mathcal{T}(\tau_g)$, which captures both relativistic clock-rate differences and signal propagation effects. The objective of the estimator is to reconstruct, at the receiver, an estimate of the generation time expressed in the RX time coordinate, $\hat{t}_g(\tau_g^{(n)})$, using only the observed timestamp/arrival-time pairs. Once such an estimate is available, the pAoI at reception is formed as

$$\hat{\Delta}_n \triangleq t_r^{(n)} - \hat{t}_g(\tau_g^{(n)}).$$

Local polynomial approximation of the time-transfer mapping: Under the weak-field and slow-variation assumptions, the time-transfer mapping $\mathcal{T}(\cdot)$ is smooth and can be locally approximated over a finite observation window by a low-order polynomial [7]. Specifically, we model

$$\hat{t}_r(\tau) = a_0 + a_1\tau + a_2\tau^2 + \ldots + a_p\tau^p. \tag{11}$$

Coefficient estimation via least squares: Given a sliding window of N received updates $\{(\tau_g^{(i)}, t_r^{(i)})\}_{i=n-N+1}^{n}$, the

```
Require: Polynomial degree $p$; window size $N \geq p+1$; stream of received updates $\{(\tau_g^{(n)}, t_r^{(n)})\}$
Ensure: pAoI estimate $\hat{\Delta}_n$ at each reception
Initialize $\hat{t}_g^{(0)} \leftarrow 0$
Maintain a sliding window $\mathcal{W}_n = \{(\tau_g^{(i)}, t_r^{(i)})\}_{i=n-N+1}^{n}$
if $|\mathcal{W}_n| < N$ then
    return (insufficient samples)
Construct Vandermonde matrix $\mathbf{X}$ from timestamps $\tau_g^{(i)}$
Stack observation vector $\mathbf{t}_r = [t_r^{(n-N+1)}, \dots, t_r^{(n)}]^T$
Compute polynomial coefficients $\hat{\mathbf{a}} \leftarrow (\mathbf{X}^T\mathbf{X})^{-1}\mathbf{X}^T\mathbf{t}_r$
Evaluate local time-transfer rate:
    $\hat{\rho}_n \leftarrow \sum_{m=1}^{p} m\,\hat{a}_m \left(\tau_g^{(n)}\right)^{m-1}$
Update generation-time estimate:
    $\hat{t}_g^{(n)} \leftarrow \hat{t}_g^{(n-1)} + \hat{\rho}_n \left(\tau_g^{(n)} - \tau_g^{(n-1)}\right)$
Compute pAoI estimate:
    $\hat{\Delta}_n \leftarrow t_r^{(n)} - \hat{t}_g^{(n)}$
```

Figure 4. pAoI Polynomial Estimation under General Relativity.

receiver estimates the polynomial coefficients by OLS. Defining the observation vector $\mathbf{t}_r$ and the Vandermonde design matrix $\mathbf{X}$ constructed from the timestamps $\tau_g^{(i)}$, the coefficient estimate is:

$$\hat{\mathbf{a}} = (\mathbf{X}^T\mathbf{X})^{-1}\mathbf{X}^T\mathbf{t}_r,$$

provided that $N \geq p+1$ and that the timestamps in the window are distinct.

Reconstruction of the generation-time mapping: The derivative of the fitted polynomial yields an estimate of the local rate at which RX time evolves with respect to TX proper time:

$$\hat{\rho}_n \triangleq \frac{d}{d\tau}\hat{t}_r(\tau)\bigg|_{\tau=\tau_g^{(n)}} = \sum_{m=1}^{p} m\,\hat{a}_m \left(\tau_g^{(n)}\right)^{m-1}.$$

This quantity represents the instantaneous time-transfer rate between TX timestamps and RX time, incorporating all relativistic and propagation effects. The receiver reconstructs the generation time expressed in the RX time coordinate by integrating the estimated local rate. In discrete time, this is performed recursively as

$$\hat{t}_g^{(n)} = \hat{t}_g^{(n-1)} + \hat{\rho}_n \left(\tau_g^{(n)} - \tau_g^{(n-1)}\right),$$

with initialization $\hat{t}_g^{(0)} = 0$ at the synchronization event.

pAoI estimation: Finally, the pAoI at reception time $t_r^{(n)}$ is estimated as

$$\hat{\Delta}_n = t_r^{(n)} - \hat{t}_g^{(n)}.$$

The complete estimation procedure is summarized in Figure 4.

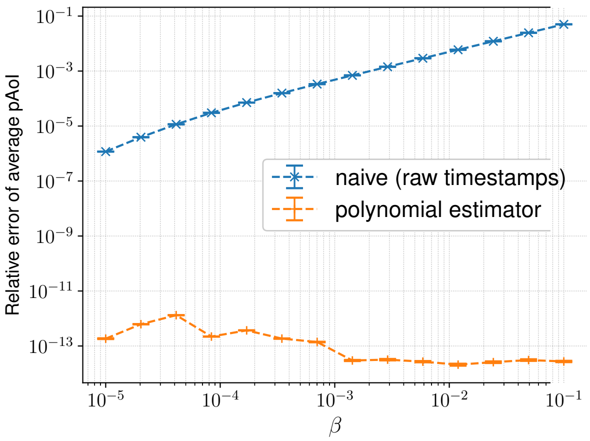

Figure 5. Estimated pAoI by Figure 3 vs Naive relative error.

TABLE I. SIMULATION PARAMETERS FOR THE SPECIAL-RELATIVISTIC CONSTANT-VELOCITY SCENARIO.

Parameter	**Value**
Polynomial degree p	2
Update generation rate λ_{TX}	2 Hz
Observation window size N	120 samples
Update generation process	Poisson process
Timestamp noise std. σ_t	1 ns

V. NUMERICAL RESULTS

In this section, we present our simulation studies. All plots involving simulations include a sufficient warm-up period before measurements are taken. Confidence intervals are shown, except where they are too tight to show at 95% confidence.

To evaluate estimator performance across relativistic regimes, we simulate the special-relativistic constant-velocity scenario introduced in Section III. The transmitter generates timestamped updates according to a Poisson process in its proper time with average rate λ_{TX}, and each update carries its generation timestamp τ_g. We chose to use a Poissonian generation process as it is memoryless, thus modeling independent single transmissions; the estimator itself is generation process agnostic, as long as the process is stationary and ergodic. Updates propagate over a LOS channel, and the receiver observes the corresponding reception times t_r in its own reference frame, distorted by relativistic time dilation and corrupted by Additive White Gaussian timestamp Noise (AWGN) with standard deviation σ_{t_r}.

We compare two receiver-side pAoI estimation strategies: (i) a naive approach that directly interprets transmitted timestamps in the receiver frame, and (ii) the polynomial AoI estimator described in Figure 3. To the best of our knowledge, no existing work addresses the estimation of AoI under relativistic time distortion. The polynomial estimator operates on a sliding window of N received updates and locally approximates the mapping between transmitted timestamps and reception times

ISBN: 978-1-68558-391-0

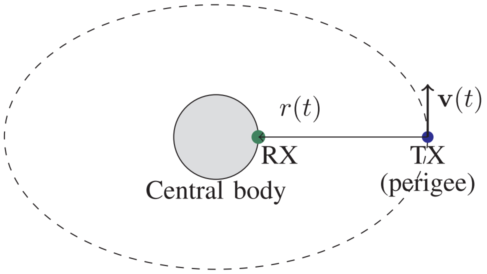

Figure 6. Simulation geometry for the general-relativistic orbital scenario.

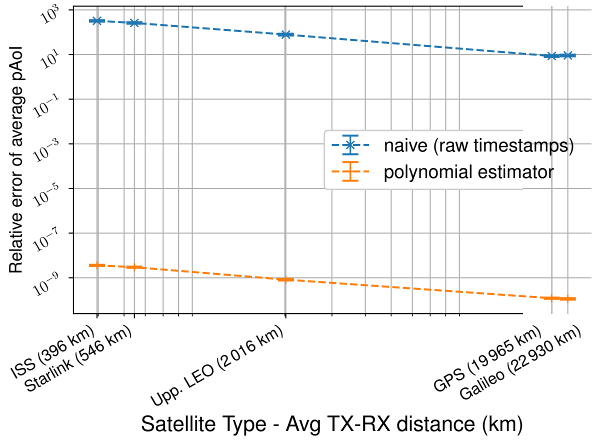

Figure 7. Estimated pAoI by the Algorithm in Figure 4 vs Naive relative error under general-relativistic time distortion. pAoI is presented vs the average altitude of TX. The most common type of satellite at that altitude is presented as well as a label.

TABLE II. SIMULATION PARAMETERS FOR THE GENERAL-RELATIVISTIC ORBITAL SCENARIO.

Parameter	**Value**
Gravitational parameter μ	$3.986 \times 10^{14}\ \mathrm{m^3/s^2}$
Central radius R	6 371 km
Orbital eccentricity e	0.01
Perigee speed ratio $\beta_p = v_p/c$	see Table III
Update generation rate λ_{TX}	2 Hz
Update generation process	Poisson process
Observation window size N	200 samples
Polynomial degree	3
Timestamp noise std. σ_t	1 ns

TABLE III. ORBITAL REGIMES MAPPING β_p TO PERIGEE (h_p) AND APOGEE (h_a) ALTITUDE FOR THE SIMULATION IN FIGURE 7.

Typical usage	β_p	h_p [km]	h_a [km]
ISS	2.585×10^{-5}	332.0	467.4
Starlink	2.557×10^{-5}	480.4	618.9
Upper LEO	2.325×10^{-5}	1 915.9	2 083.3
GPS GNSS	1.305×10^{-5}	19 933.0	20 464.4
Galileo GNSS	1.237×10^{-5}	22 924.6	23 516.4

by a polynomial of degree p. From this approximation, the receiver reconstructs the generation time expressed in its own reference frame and computes the estimated pAoI by comparing it with the reception time.

The normalized transmitter speed β is swept logarithmically from values representative of GNSS systems to increasingly relativistic regimes. For each β, the simulation is allowed to reach steady state before collecting measurements. The parameters used in this numerical study are reported in Table I.

Figure 5 compares the true average pAoI with estimates obtained using the naive timestamp comparison and the proposed polynomial estimator. The metric used is the relative error of the average pAoI with respect to the true average pAoI, i.e.,

$$\frac{|\mathbb{E}[\hat{\Delta}] - \mathbb{E}[\Delta]|}{\mathbb{E}[\Delta]} .$$

Notice that said error is dimensionless.

The results show that the naive approach consistently overestimates or underestimates pAoI depending on the relative motion, while the estimator closely tracks the true value. Naive AoI evaluation fails to account for time dilation, whereas the proposed estimator successfully recovers the correct pAoI by exploiting temporal structure across updates.

To test the pAoI estimator described in Figure 4, we consider a concrete instantiation of the general-relativistic model introduced in Section IV-A, corresponding to a transmitter moving on a Keplerian geosynchronous orbit around Earth as the central body (Figure 6). Note that RX and TX are assumed to be always in direct LOS, being TX in geosynchronous orbit around Earth, thus the distance separating them is the instantaneous radius of TX orbit minus the radius of the Earth, i.e., the minimum euclidean distance between them. No atmospheric effects are introduced – i.e., the transmission medium is vacuum; signal propagation occurs through vacuum along null trajectories of the spacetime geometry.

A simulation run is initialized with the following parameters:

- μ: gravitational parameter of Earth, i.e., the product of the gravitational constant G and the mass of Earth (RX and TX masses are considered negligible with respect to the mass of the Earth).
- R: radius of the Earth: $R \approx 6\,371$ km.
- $e \in [0, 1)$: orbital eccentricity of the transmitter, i.e., how much the orbit deviates from a perfect circle.
- β_p: normalized perigee speed, i.e., $\beta_p = v_p/c$, i.e., the fastest orbital speed TX achieves when at the perigee; along with the previous parameters it is sufficient to completely define TX orbit at any point in relative time. Note that, given μ, e and R, the normalized perigee speed is upper bounded, i.e., $0 \leq \beta_p \leq \frac{1}{c}\sqrt{\frac{\mu(1+e)}{R}} \approx 2.8\times10^{-5}$.
- λ_{TX}: update generation rate in the transmitter proper time. As per the Special Relativity case, we chose to generate updates according to a Poissonian Process.
- σ_{t_r}: standard deviation of additive reception timestamp noise at the receiver.
- p: polynomial degree used by the estimator.
- N: estimator window size (number of most recent updates

Copyright (c) IARIA, 2026. ISBN: 978-1-68558-391-0

used for fitting).

The input parameter β_p completely defines the instantaneous altitude of TX, the complete mapping is presented in Table III, ranging from the International Space Station (ISS) to Galileo GNSS altitude.

The life cycle of a generated update goes through the following steps:

1) The update is generated at time τ_n – as measured by the clock onboard TX – and timestamped.
2) Kepler's equation is solved to find the instantaneous eccentric anomaly $E(\tau_n)$:

$$E(\tau_n) - e\sin\left(E(\tau_n)\right) = \tau_n\sqrt{\frac{\mu}{a^3}}\,,$$

where a is the semi-major axis of TX orbit:

$$a = \frac{\mu(1+e)}{v_p^2(1-e)}\,, \tag{12}$$

and v_p is the perigee speed:

$$v_p = \beta_p c\,.$$

3) The instantaneous orbital distance $r(\tau_n)$ is then obtained as:

$$r(\tau_n) = a\big(1 - e\cos\left(E(\tau_n)\right)\big) - R\,.$$

4) From the previous, the instantaneous orbital speed is computed using the vis-viva equation:

$$v(\tau_n) = \sqrt{\mu\left(\frac{2}{r(\tau_n)} - \frac{1}{a}\right)}\,.$$

5) The receiver is assumed to be inertial and located at a fixed position on the surface of the Earth, defining the reference frame in which the pAoI is evaluated. Gravitational effects are modeled through a static Newtonian potential:

$$\Phi(r) = -\mu/r\,, \tag{13}$$

where μ is the standard gravitational parameter of Earth (the central body) and r denotes the instantaneous TX-RX distance. Under the weak-field, slow-motion approximation, and the fact that we assumed continuous LOS, the mapping between proper time and receiver coordinate time is obtained by integrating the rate [5]:

$$\frac{dt}{d\tau} \approx 1 - \frac{\Phi(r)}{c^2} - \frac{v^2}{2c^2}\,.$$

By substituting (13) in the previous we finally obtain the time dilation rate:

$$\frac{dt}{d\tau} \approx 1 + \frac{\mu}{r(\tau_n)c^2} - \frac{v(\tau_n)^2}{2c^2}\,, \tag{14}$$

that, integrated, gives us the true mapping function $\mathcal{T}(\tau_g)$ (10), used to calculate the simulated true reception time $t_g^{(n)}$.

6) The propagation delay is modeled as a LOS radial delay, as we always assume LOS. We also add AWGN $w_n \sim \mathcal{N}(0, \sigma_{t_r}^2)$; the time observed at reception in the RX frame of reference becomes:

$$\hat{t}_r^{(n)} = t_g^{(n)} + \frac{r(\tau_n)}{c} + w_n\,.$$

7) Finally RX, adds $\hat{t}_r^{(n)}$ to the observation window, and uses Figure 4 – when there are sufficient observations, i.e., $n \geq N \geq p+1$ – to produce the current estimation of the true pAoI $\hat{\Delta}(\tau_n)$.

To ensure numerical stability of the least-squares fitting procedure, the transmitter timestamps τ_g within each window are centered and normalized prior to constructing the polynomial regression matrix. This avoids the severe ill-conditioning associated with Vandermonde matrices built on unscaled time variables [19] and ensures robust coefficient estimation even for higher-order polynomials. To avoid initialization bias, the estimator is explicitly anchored when the first complete observation window becomes available by initializing the estimated generation time to the corresponding propagation-corrected observation. Subsequent estimates are obtained recursively by integrating the estimated local clock rate. This approach prevents spurious offsets due to estimator warm-up and ensures that the estimated pAoI does not suffer from numerical artifacts.

In Figure 7, we plotted the estimated pAoI by Figure 4 vs true AoI for different type of satellites (see Table III). The parameters used in the numerical study are described in Table II. The estimator outperforms the naive approach by several orders of magnitude in all regimes. Note that, due to (12), there is a square inverse proportionality between the average altitude of TX and the perigee speed.

The absolute error levels in Figures 5 and 7 are not directly comparable: the special-relativistic mapping is linear and closed-form, yielding a well-conditioned problem, whereas the general-relativistic mapping is nonlinear and time-varying, requiring local approximation and numerical integration under significantly more challenging conditions. Additionally, note that the naive estimator exhibits markedly different behavior in the two scenarios. Specifically, constant distortions under special relativity induce only a linear bias, leading to bounded estimation errors; in contrast, time-varying distortions under general relativity are integrated over the observation horizon, leading to cumulative errors.

VI. CONCLUSION AND FUTURE WORK

This paper established a relativistic perspective on AoI, showing that information freshness is fundamentally affected by time dilation due to relative motion and gravity. We demonstrated that naive timestamp comparison leads to systematic errors in pAoI evaluation, even at low relative speeds. To address this, we proposed polynomial estimators that reconstruct the generation time in the receiver reference frame using only timestamped updates. For special relativity, the proposed estimator consistently outperforms the naive method across all velocity regimes. The framework was further extended to general relativity using a weak-field approximation, enabling accurate pAoI recovery under combined gravitational and kinematic distortions. Numerical results validate the effectiveness of the proposed approach and highlight the importance of relativistic modeling in high-mobility and space-based communication systems.

Several directions emerge naturally from this work. First, while the present analysis relies on weak-field approximations, extending the framework to strong gravitational fields would enable the study of information freshness in more extreme environments, such as deep-space missions or communication near compact astrophysical objects. Second, the general-relativistic model considered here assumes non-relativistic orbital velocities; incorporating regimes in which velocities approach the speed of light would require abandoning the weak-field expansion and adopting a fully relativistic spacetime description, potentially revealing qualitatively new AoI behaviors. Finally, this paper focused primarily on mean AoI and pAoI. An important extension is the characterization of the full AoI distribution under relativistic time distortions, which would allow the analysis of threshold-based freshness violations and quality-of-service guarantees. Such a distributional perspective is particularly relevant for safety-critical and real-time systems, where rare but severe AoI excursions can be as important as average performance.

ACKNOWLEDGMENT

This work was sponsored in part by the Excellence Center at Linköping-Lund in Information Technology (ELLIIT) Sweden.

REFERENCES

[1] S. Kaul, R. Yates, and M. Gruteser, “Real-time status: How often should one update?”, in *Proc. 2012 IEEE INFOCOM*, Mar. 2012, pp. 2731–2735. DOI: 10.1109/INFCOM.2012.6195689

[2] M. Costa, M. Codreanu, and A. Ephremides, “Age of information with packet management”, in *Information Theory (ISIT), 2014 IEEE International Symposium on*, Jun. 2014, pp. 1583–1587. DOI: 10.1109/ISIT.2014.6875100

[3] A. Kosta, N. Pappas, and V. Angelakis, “Age of information: A new concept, metric, and tool”, *Foundations and Trends in Networking*, vol. 12, no. 3, pp. 162–259, 2017.

[4] N. Pappas, M. A. Abd-Elmagid, B. Zhou, W. Saad, and H. S. Dhillon, *Age of Information: Foundations and Applications*. Cambridge University Press, 2023, ISBN: 9781108950275.

[5] N. Ashby, “Relativity in the global positioning system”, *Living Reviews in Relativity*, vol. 6, no. 1, pp. 1–45, Jan. 2003, ISSN: 1433-8351. DOI: 10.12942/lrr-2003-1

[6] K. L. Senior, J. R. Ray, and R. L. Beard, “Characterization of periodic variations in the gps satellite clocks”, *GPS solutions*, vol. 12, no. 3, pp. 211–225, 2008.

[7] H. Ge, B. Li, T. Wu, and S. Jiang, “Prediction models of gnss satellite clock errors: Evaluation and application in ppp”, *Advances in Space Research*, vol. 68, no. 6, pp. 2470–2487, 2021.

[8] Z. Gao, A. Liu, C. Han, and X. Liang, “Non-orthogonal multiple access-based average age of information minimization in leo satellite-terrestrial integrated networks”, *IEEE Transactions on Green Communications and Networking*, vol. 6, no. 3, pp. 1793–1805, 2022. DOI: 10.1109/TGCN.2022.3159559

[9] Y. Li, Y. Xu, Q. Zhang, and Z. Yang, “Age-optimized multihop information update mechanism on the leo satellite constellation via continuous time-varying graphs”, *IEEE Internet of Things Journal*, vol. 10, no. 8, pp. 7189–7203, 2023. DOI: 10.1109/JIOT.2022.3229028

[10] C.-Y. Lin and W. Liao, “Energy-aware age of information (aoi) minimization for internet of things in noma-based leo satellite networks”, in *2024 IEEE 99th Vehicular Technology Conference (VTC2024-Spring)*, 2024, pp. 1–5. DOI: 10.1109/VTC2024-Spring62846.2024.10683037

[11] D. Zhang et al., “Age of information variation of leo satellite-terrestrial uplink transmissions”, *IEEE Transactions on Vehicular Technology*, vol. 74, no. 6, pp. 9645–9655, 2025. DOI: 10.1109/TVT.2025.3540572

[12] H. Zarini, S. M. Kazemi, M. Sookhak, E. Uysal, and S. Chatzinotas, “Age of information in leo satellite communications supported by bd-ris”, in *ICC 2025 - IEEE International Conference on Communications*, 2025, pp. 1–6. DOI: 10.1109/ICC52391.2025.11161975

[13] B. Gabr and M. A. Kishk, “Statistical analysis for average peak age of information in leo satellite-enabled iot”, in *2025 IEEE 101st Vehicular Technology Conference (VTC2025-Spring)*, 2025, pp. 1–6. DOI: 10.1109/VTC2025-Spring65109.2025.11174394

[14] M. Liao et al., “Multihop age-of-information-enhanced routing mechanism for delay-sensitive service in the leo satellite networks”, *IEEE Internet of Things Journal*, vol. 12, no. 23, pp. 51 168–51 181, 2025. DOI: 10.1109/JIOT.2025.3612043

[15] B. Gabr and M. A. Kishk, “Performance analysis of average peak age of information in leo satellite-enabled iot networks”, *IEEE Transactions on Wireless Communications*, vol. 25, pp. 5186–5199, 2026. DOI: 10.1109/TWC.2025.3616774

[16] L. Badia and A. Munari, “Satellite intermittent connectivity and its impact on age of information for finite horizon scheduling”, in *2025 12th Advanced Satellite Multimedia Systems Conference and the 18th Signal Processing for Space Communications Workshop (ASMS/SPSC)*, 2025, pp. 1–8. DOI: 10.1109/ASMS/SPSC64465.2025.10946056

[17] W. Qin et al., “The benefits of receiver clock modelling in satellite timing”, *Sensors*, vol. 21, no. 2, 2021, ISSN: 1424-8220. DOI: 10.3390/s21020466

[18] D. C. Rife and R. R. Boorstyn, “Single tone parameter estimation from discrete-time observations”, *IEEE Transactions on Information Theory*, vol. 20, no. 5, pp. 591–598, 1974.

[19] V. Y. Pan, “How bad are vandermonde matrices?”, *SIAM Journal on Matrix Analysis and Applications*, vol. 37, no. 2, pp. 676–694, 2016.

ISBN: 978-1-68558-391-0

Metamaterial-Inspired Highly Compact Wearable Antenna for 406 MHz Cospas-Sarsat Personal Locator Beacons (PLBs)

Mehmet Doğan
Telecommunications Engineering
Istanbul Technical University
Istanbul, Türkiye
E-Mail: doganm16@itu.edu.tr

Mesut Kartal
Electronics and Communication Engineering
Istanbul Technical University
Istanbul, Türkiye
E-Mail: kartalme@itu.edu.tr

***Abstract*—This paper proposes a highly miniaturized wearable antenna for 406 MHz Cospas-Sarsat Personal Locator Beacons (PLBs). To overcome the physical size constraints of the 74 cm wavelength, a metamaterial-inspired design technique is employed. The design achieves approximately 95 percent size reduction while maintaining the required radiation efficiency for satellite uplink. Results demonstrate that the antenna is designed/aimed to mitigate the frequency detuning caused by human body proximity. This compact, flexible solution ensures reliable signal transmission in critical search and rescue operations.**

Keywords-wearable antenna; metamaterial; 406 MHz; Cospas-Sarsat; Personal Locator Beacon; miniaturization.

I. INTRODUCTION

The international Cospas-Sarsat (Cosmicheskaya Sistema Poiska Avariynyh Sudov / Search And Rescue Satellite-Aided Tracking) satellite system has been instrumental in saving thousands of lives worldwide by detecting and locating emergency beacons since 1984. This satellite communication network is exclusively reserved for emergency distress signals and is accessed through specific devices depending on the domain: Emergency Locator Transmitters (ELTs) in aviation, Emergency Position-Indicating Radio Beacons (EPIRBs) in maritime environments, and Personal Locator Beacons (PLBs) for individual use [1]. Currently, most PLBs available on the market are housed in bulky, walkie-talkie-style form factors. Transitioning these life-saving devices into a wearable, ultra-lightweight form would significantly enhance their ease of use, portability, and global adoption among outdoor enthusiasts and personnel in hazardous environments.

However, realizing a wearable PLB presents a significant physical challenge due to the operating frequency. Cospas-Sarsat beacons transmit at 406 MHz in the UHF band, which corresponds to a free-space wavelength of approximately 74 cm. Designing an efficient antenna that fits on the human body at this wavelength requires advanced miniaturization techniques.

Several approaches have been explored in the literature to achieve antenna miniaturization in the UHF band. One traditional method involves the use of high dielectric constant substrates to reduce the physical dimensions of the antenna [2][3]. Unfortunately, this approach inherently traps the electromagnetic fields within the substrate, leading to a substantial degradation in overall antenna gain and radiation efficiency. Another commonly utilized method is the implementation of fractal geometries to increase the effective electrical length within a constrained physical area [4]. While fractal antennas can achieve a size reduction of approximately 30 percent, their complex structures are costly to manufacture and introduce severe reliability and yield issues in large-scale mass production.

To overcome these critical limitations, this paper adopts a metamaterial-inspired antenna design approach, a concept pioneered by Ziolkowski [5]. Unlike previous miniaturization methods, metamaterial-inspired structures offer extreme size reduction which is often exceeding 80 percent, while maintaining a high degree of implementation simplicity and manufacturing cost-effectiveness. By leveraging this technique, this study proposes a compact and flexible wearable antenna tailored specifically for 406 MHz Cospas-Sarsat applications, ensuring reliable performance and resilient signal transmission. In order to demonstrate the suitability of the metamaterial-inspired approach originally proposed in [5] for wearable electronics, this study investigates its implementation on a flexible Polyimide substrate and evaluates the resulting performance through full-wave simulations.

Despite the significant advantages of extreme size reduction, the metamaterial-inspired approach inherently presents certain limitations. The highly reactive nature of electrically small antennas makes them particularly sensitive to environmental factors. In wearable applications, the close proximity of the human body can introduce frequency detuning and alter radiation characteristics [6]. Additionally, extreme miniaturization typically yields a narrow operational bandwidth and necessitates careful assessment of Specific Absorption Rate (SAR) compliance to ensure human safety [7].

The remainder of this paper is organized as follows: Section II details the antenna design and methodology, encompassing the theoretical foundation of the near-field resonant parasitic element, the flexible wearable configuration, and the internal impedance matching strategy. Section III presents and discusses the full-wave electromagnetic simulation results, evaluating the return loss, VSWR, and far-field radiation patterns in a free-space environment. Finally, Section IV concludes the paper and

ISBN: 978-1-68558-391-0

outlines future work regarding human body phantom simulations and physical prototyping.

II. ANTENNA DESIGN AND METHODOLOGY

This section presents the comprehensive design methodology of the proposed metamaterial-inspired antenna, detailing its theoretical framework, material properties, and specific structural configuration.

A. Theoretical Foundation

The core of the proposed miniaturization technique is based on the metamaterial-inspired near-field resonant parasitic concept, initially introduced as the Z antenna. To bypass the extreme physical constraints of the 74 cm wavelength at 406 MHz, the design employs an electrically small, Z-shaped element [5]. A lumped element inductor connects the two halves of this structure across a central gap. The theoretical framework dictates that the resonance frequency f_{res} of the antenna is governed by its effective inductance L_{eff} and effective capacitance C_{eff}, as expressed in the following equation [5]:

$$f_{res} = (2\pi\sqrt{L_{eff}\, C_{eff}})^{-1} \tag{1}$$

The metamaterial-inspired nature of the Z-shaped element stems from its operation as a Near-Field Resonant Parasitic (NFRP) structure. At subwavelength dimensions, this loaded element acts analogously to a single metamaterial unit cell. Instead of relying on a bulk periodic medium, the Z-shaped parasitic resonator strongly couples to the highly reactive, non-radiating near-fields generated by the aperture feed. This strong electromagnetic coupling creates a highly localized artificial resonance that effectively neutralizes the inherently high capacitive reactance of the electrically small structure. Consequently, the parasitic element acts as an efficient radiator, transferring energy to the far-field while internally matching the impedance.

Because the physical dimensions of the parasitic structure are fixed, C_{eff} remains constant, and L_{eff} is primarily dominated by the introduced lumped element inductor. The resonant frequency can be precisely tuned to the required 406 MHz Cospas-Sarsat band simply by selecting the appropriate inductance value, enabling extreme miniaturization without expanding the physical footprint [8] [9].

B. Proposed 406 MHz Wearable Configuration

Unlike traditional UHF designs that rely on rigid, high-permittivity substrates, the proposed antenna is fabricated on a flexible Polyimide Printed Circuit Board (PCB) substrate with a relative permittivity (ε_r) of 3.5. This highly conformable and low-loss material ensures the device can comfortably fit on the human body for PLB applications. Furthermore, to guarantee superior performance, extreme flexibility, and high resistance to oxidation in harsh outdoor environments, gold is utilized as the conductive material for the antenna arms [10].

The antenna system comprises two primary layers. The top layer features the highly compact, gold-based Z-shaped parasitic radiator. In a significant departure from the direct coax-fed monopoles utilized in the foundational experimental validations of UHF Z antennas, this design employs an aperture coupling feeding mechanism [5]. The feeding line is isolated on the bottom layer, coupling electromagnetic energy through a strategically placed slot in the shared ground plane. This aperture-coupled approach offers an additional degree of freedom in impedance matching and enhances the isolation between the radiating element and the feed network. This architectural choice is crucial for mitigating frequency detuning effects caused by the proximity of the human body, a major challenge in wearable devices.

C. Impedance Matching and Efficiency

Experimental verifications of similar UHF metamaterial-inspired antennas have proven that the near-field resonant parasitic element effectively acts as an internal matching network [8][9][11]. By appropriately tuning the central lumped inductor, the input impedance of the highly reactive electrically small antenna is matched to a standard 50Ω source without the need for any bulky external matching circuits. This approach not only shrinks the physical size by approximately 95 percent but also preserves the high radiation efficiency necessary for reliable 406 MHz satellite uplink in critical search and rescue operations.

D. Antenna Geometry and Dimensions

The overall physical footprint of the designed antenna is remarkably compact, utilizing a square Polyimide substrate with dimensions of exactly 30 x 30 mm. This extreme size reduction highlights the effectiveness of the metamaterial-inspired approach for the 74 cm wavelength constraint.

As illustrated in the top view of the antenna (see Figure 1), the gold-plated Z-shaped parasitic element dominates the top layer. To achieve the desired resonance exactly at the 406 MHz frequency, a 60 nH lumped element inductor is strategically placed and soldered across the central gap of the radiating arms. The bottom layer of the substrate (see Figure 2) houses the vertical feedline structure responsible for the aperture coupling mechanism.

ISBN: 978-1-68558-391-0

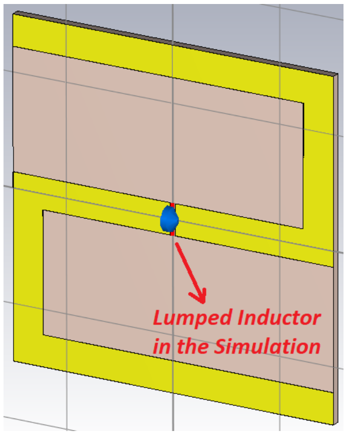

Figure 1. Top view of the proposed metamaterial-inspired wearable antenna, illustrating the gold-plated Z-shaped element and the central lumped inductor. Please note that there is a slot gap directly underneath the lumped inductor.

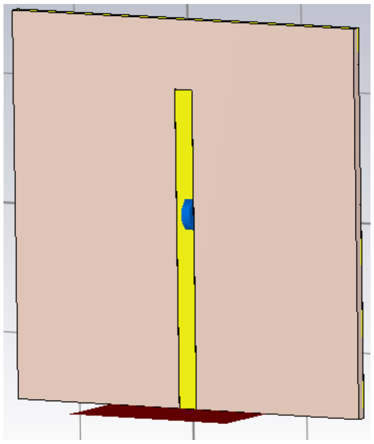

Figure 2. Bottom view of the antenna, detailing the isolated feedline structure used for the aperture coupling mechanism. The area surrounding the antenna's RF Port Excitation is represented by the Ground Plane, which is colored brown in the simulation.

The integration of the top layer's near-field resonant parasitic element with the bottom layer's isolated feedline structure establishes a highly compact and robust design. This precise architectural alignment is essential for achieving the targeted 406 MHz resonance within the constrained footprint , providing a foundation for the numerical performance analysis presented in the subsequent section.

III. SIMULATION RESULTS AND DISCUSSION

To evaluate the performance of the proposed wearable PLB antenna, full-wave electromagnetic simulations were conducted. The numerical analysis was performed using CST Studio Suite Tool – Version 2024, utilizing open boundary conditions to accurately emulate a free-space environment. To precisely model the thin flexible Polyimide substrate, the sub-millimeter coupling aperture, and the strong near-field interactions around the lumped inductor, an adaptive meshing technique with local mesh refinement was employed. The primary parameters investigated in this study were the return loss (S_{11}), Voltage Standing Wave Ratio (VSWR) and the far-field radiation characteristics.

A. *Return Loss*

The metamaterial-inspired design, leveraging the central lumped inductor for internal impedance matching, demonstrates a distinct and sharp resonance exactly at the 406 MHz Cospas-Sarsat operating frequency. As shown in Figure 3, the simulated return loss achieves a minimum value of -12 dB, safely exceeding the standard -10 dB threshold.

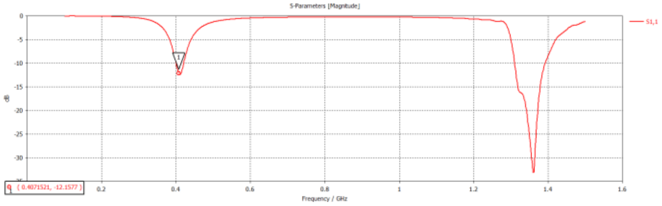

Figure 3. Simulated return loss S_{11} of the proposed metamaterial-inspired wearable antenna, demonstrating a resonance peak of -12.15 dB at 406 MHz band.

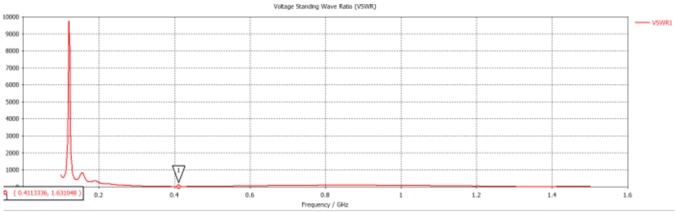

Figure 4. Simulated Voltage Standing Wave Ratio (VSWR) of the proposed antenna, indicating a well-matched value of 1.63 in the operating band.

Furthermore, to evaluate the power delivery and impedance matching quality, the VSWR of the antenna was analyzed. As depicted in Figure 4, the antenna exhibits a VSWR of 1.63 near the resonance frequency. Since a VSWR value of less than 2.0 is considered highly acceptable for practical antenna operations, this result is a strong indicator of successful miniaturization. These findings confirm that the aperture-coupled feeding mechanism, combined with the near-field resonant parasitic element, successfully matches the highly reactive input impedance of the heavily miniaturized antenna to a 50Ω source without requiring any bulky external matching networks.

B. *Radiation Pattern and Gain*

A critical challenge in extreme antenna miniaturization is the inherent degradation of radiation efficiency and gain. However, despite achieving an approximately 95 percent size reduction relative to the 74 cm free-space wavelength, the proposed antenna exhibits a highly stable omnidirectional radiation pattern suitable for satellite communications. The utilization of a low-loss Polyimide substrate and highly conductive gold arms ensures that the resistive losses are minimized. The simulation results indicate a peak realized gain of 1.1 dBi and a robust radiation efficiency of 94.4 percent.

IV. CONCLUSION AND FURTHER WORK

This paper has successfully demonstrated that the metamaterial-inspired antenna architecture, originally proposed by Ziolkowski, provides a highly viable framework for wearable electronic implementations aimed at demanding satellite communication systems.

Furthermore, considering the device’s proximity to the user, ensuring electromagnetic safety through rigorous SAR compliance is a fundamental requirement. Consequently, high-fidelity simulations utilizing human body phantoms will be prioritized to guarantee that the design meets international safety standards, serving as a critical prerequisite for the successful implementation and testing of the final physical prototype. By adapting this foundational concept into a highly compact, wearable configuration specifically for 406 MHz Cospas-Sarsat PLBs, this study demonstrates the promising feasibility of achieving extreme miniaturization while delivering the desired radiation efficiency.

The designed antenna overcomes the physical size constraints of the 74 cm UHF wavelength. Our free-space simulation results validate that the antenna shrinks the physical footprint by approximately 95 percent, achieving a stable return loss of -12.15 dB and maintaining the excellent internal impedance matching and radiation characteristics essential for critical search and rescue satellite uplinks.

While the free-space performance strongly validates this miniaturization approach for satellite applications, the practical deployment of wearable antennas requires rigorous validation against human body proximity effects.

Therefore, future work will focus on extensive simulations utilizing human body phantoms to evaluate frequency detuning and SAR compliance. Subsequently, a physical prototype of the antenna will be fabricated, and laboratory measurements will be conducted to experimentally verify the simulated results.

ACKNOWLEDGMENT

This work was supported by Pharus Tech Inc., headquartered in Ankara, Türkiye.

REFERENCES

[1] W. Wang and S. Wang, “Overview of the international satellite-based COSPAS-SARSAT system,” Space Information Networks (SINC 2018), CCIS 972, pp. 52–61, 2019, doi: 10.1007/978-981-13-5937-8_7.

[2] M. Mirzaee and Y. Kim, “Antenna miniaturization using high-permittivity and magneto-dielectric substrates in VHF-UHF bands: A comparative study,” 2021 IEEE International Symposium on Antennas and Propagation and North American Radio Science Meeting (APS/URSI), pp. 487–488, 2021, doi: 10.1109/APS/URSI47566.2021.9704069,

[3] M. Aldrigo et al., “Numerical and experimental characterization of a button-shaped miniaturized UHF antenna on magneto-dielectric substrate,” International Journal of Microwave and Wireless Technologies, vol. 5, special issue 3, pp. 231–239, 2013, doi: 10.1017/S1759078713000445.

[4] A. Karmakar, “Fractal antennas and arrays: a review and recent developments,” International Journal of Microwave and Wireless Technologies, vol. 13, pp. 173–197. July 2020, doi: 10.1017/S1759078720000963

[5] R. W. Ziolkowski, “An Efficient, electrically small antenna designed for VHF and UHF applications,” IEEE Antennas and Wireless Propagation Letters, vol. 7, pp. 217-220, Feb. 2008, doi: 10.1109/LAWP.2008.921635.

[6] P. Salonen and Y. Rahmat-Samii, “Textile antennas: Effects of antenna bending on input matching and impedance bandwidth,” IEEE Aerospace and Electronic Systems Magazine, vol. 22(12), pp. 18–22, Jan. 2008, doi: 10.1109/MAES.2007.4408597.

[7] Y. Hao et al., "Antennas and propagation for body centric wireless communications," IEEE/ACES International Conference on Wireless Communications and Applied Computational Electromagnetics 2005, pp. 586-589, April 2005, doi: 10.1109/WCACEM.2005.1469656.

[8] R. W. Ziolkowski, P. Jin, J. A. Nielsen, M. H. Tanielian, and C. L. Holloway, “Experimental verification of Z antennas at UHF frequencies,” IEEE Antennas and Wireless Propagation Letters, vol. 8, pp. 1329-1333, Oct. 2009, doi: 10.1109/LAWP.2009.2038180.

[9] P. Jin and R. W. Ziolkowski, “Broadband, efficient, electrically small metamaterial-inspired antennas facilitated by active near-field resonant parasitic elements,” IEEE Antennas and Wireless Propagation Letters, vol. 58, no. 2, pp. 318-327, Feb. 2010, doi: 10.1109/TAP.2009.2037708.

[10] I. Abdel-Motaleb and S. Dittakavi, “SiC THz sensors for harsh environment applications,” Open J. Antennas Propag., vol. 9, pp. 45-55, 2021, doi:10.4236/ojapr.2021.93004.

[11] X. Jin, C. Hua, Z. Lu, and L. Liu, “A Metamaterial-inspired RFID tag antenna” 2019 International Conference on Microwave and Millimeter Wave Technology (ICMMT), May. 2019, pp. 1-3, ISBN: 978-1-7281-2168-0.

Dual-Domain Structural Interference Detection in FDMA based Satellite Communication Networks using Carrier-Aware Spectral Cursor

Sahal Mohammed M N, Abhiram N, Bhimeswara Rao M, Rath D N and Shivani K L
ISRO Telemetry Tracking and Command Network (ISTRAC)
Bangalore, India
e-mail: {sahal | bhimeswar_rao | rathdn | shivani}@istrac.gov.in
{abrm1896}@gmail.com

***Abstract*—Reliable operation of satellite communication links operating in the Frequency Division Multiple Access (FDMA) architecture requires accurate detection of spectral anomalies that may indicate interference, link outage, or carrier distortion. In dense multi-carrier environments, precise identification of interference is essential to avoid misclassifying legitimate carrier energy as anomalous behavior. Conventional automated approaches often apply uniform statistical thresholding across the entire band, making it difficult to distinguish structured carrier energy from genuine interference in heterogeneous spectral conditions. This results in either missed detections within carrier interiors or excessive false alarms near transition regions. This paper proposes a structured dual-domain interference detection framework based on explicit carrier segmentation. A hierarchical carrier-to-noise transition localization strategy with adaptive noise floor estimation first partitions the spectrum into carrier, shoulder, and transition regions. Based on this segmentation, the framework introduces two complementary analytical modules. The Carrier-Aware Spectral Cursor (CASC) is a noise-domain evaluation technique that operates within carrier-adjacent shoulder regions to detect noise floor elevation and transition anomalies. The Carrier Anomaly Detection (CAD) module is a carrier-domain structural analysis method that evaluates internal carrier symmetry and localized envelope deviations to identify distortion or intrusion. By separating noise-domain and carrier-domain logic, the proposed architecture provides a deterministic and interpretable solution for automated interference detection in multi-carrier satellite communication networks. The framework has been deployed within the ISTRAC satellite communication network, operating across geographically distributed ground stations interconnected through FDMA-SCPC architecture.**

Keywords- Satellite Communications; FDMA-SCPC Systems; Interference Detection; Carrier-Aware Spectral Cursor; Carrier Anomaly Detection.

I. INTRODUCTION

Modern satellite communication systems operate in tightly regulated and increasingly congested radio frequency environments, where maintaining spectral integrity is essential for reliable data transfer [1]. In FDMA based Single-Channel-Per-Carrier (SCPC) configurations, multiple geographically distributed ground stations share common satellite transponders within limited bandwidth [2][3].

Under nominal conditions, transponder spectra remain structurally stable and predictable. In operational environments, however, spectral deviations arise due to noise floor elevation, equipment nonlinearity, unintended emissions, or external interference [4]. If not detected in time, these anomalies degrade link margins, weaken carrier isolation, and affect overall communication reliability. Automated and robust interference detection therefore becomes essential in dense multi-carrier deployments.

The challenge is amplified in FDMA-SCPC systems, where carriers differ in bandwidth, modulation, and roll-off characteristics while operating in close spectral proximity. Legitimate carrier energy coexists with noise transitions and measurement artifacts, making interference difficult to distinguish from normal spectral variation. Subtle distortions such as intra-carrier asymmetry, localized intrusion, or gradual noise rise may not produce significant power changes yet can still impair link performance.

Traditional satellite interference monitoring has largely relied on manual spectrum inspection, fixed threshold alarms, and periodic snapshots. Early automated approaches employed power spectral density estimation and statistical energy-based thresholding techniques [5], while more recent studies explored machine learning-assisted spectrum prediction and interference detection [6]. However, multi-carrier spectra are not statistically uniform. Carrier regions exhibit structured high-energy behavior, whereas adjacent noise regions are stochastic. Uniform thresholding often produces false alarms near carrier edges and missed detections within carrier interiors. Although machine learning approaches improve sensitivity, they typically require representative training data and may lack deterministic interpretability in operational satellite systems.

To address these limitations, a structured dual-domain interference detection framework is proposed. The spectrum is first segmented into carrier and noise regions, after which carrier-domain structural assessment is performed independently from noise-domain evaluation. This separation enables consistent detection of both noise-driven and structure-driven interference while preserving interpretability in dense multi-carrier satellite transponders.

The remainder of this paper is organized as follows. Section II presents the proposed dual-domain interference detection methodology, including spectral segmentation, CASC noise-domain analysis, and CAD carrier-domain analysis. Section III discusses the experimental evaluation and detection results obtained from operational satellite transponder spectra. Finally, Section IV concludes the paper and outlines possible future extensions of the proposed framework.

ISBN: 978-1-68558-391-0

II. METHODOLOGY

The proposed methodology establishes a structured dual-domain analytical framework for deterministic interference detection in multi-carrier satellite transponder spectra by combining carrier-aware segmentation, adaptive noise-domain evaluation, and carrier-domain structural analysis.

A. System Architecture Overview

The proposed framework employs a structured dual-domain architecture for automated interference detection. Rather than treating the spectrum as a homogeneous signal field, the method explicitly separates noise and transition regions from verified carrier regions, reflecting practical RF diagnostic reasoning where noise behavior and carrier structure are interpreted independently, as illustrated in Figure 1.

Following spectral acquisition, structured segmentation establishes carrier boundaries and transition zones. Carrier center frequencies are assumed known from the operational frequency allocation plan and serve as initialization anchors for directed transition localization. Domain-specific processing is then applied within each region through the dual-path workflow shown in Figure 2, where noise-domain analysis performs adaptive baseline estimation and detection of unauthorized energy, while carrier-domain analysis evaluates internal envelope symmetry and localized structural deviations.

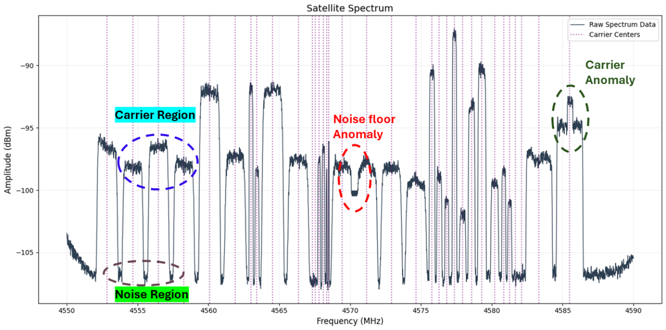

Figure 1. Typical multi-carrier satellite transponder spectrum illustrating carrier regions, noise regions, and representative noise-floor and carrier-structure anomalies.

The outputs of both domains are integrated within a unified decision stage, producing a coherent and interpretable assessment of transponder condition.

B. Data Acquisition and Pre-Processing

The entire acquisition and signal processing workflow is implemented in `Python`, leveraging `PyVISA` for remote instrument control [7] and `NumPy/SciPy` for numerical analysis [8][9]. Spectral measurements are acquired from a `Rohde & Schwarz` spectrum analyzer [10] configured for satellite transponder downlink observation. Fixed measurement parameters, including center frequency, frequency span, resolution bandwidth (RBW), and sweep resolution, are maintained to ensure repeatable and consistent acquisitions across monitoring intervals. Each sweep returns a discrete amplitude vector expressed in dBm over the configured transponder bandwidth.

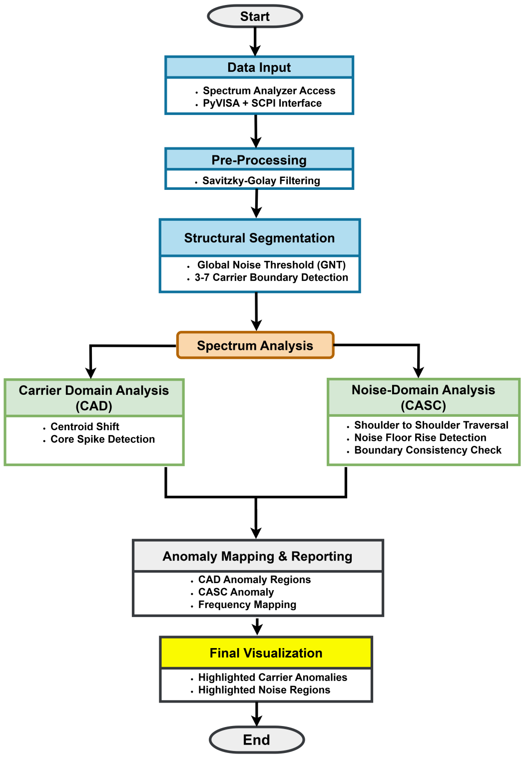

Figure 2. Proposed dual-domain structural interference detection framework with segmentation-driven CASC and CAD processing paths.

Let the acquired spectrum be represented as in (1)

$$A(f_k), \quad k = 1, 2, \ldots, N \tag{1}$$

where f_k denotes the discrete frequency bins and N is the total number of samples across the observed span.

*1) **Savitzky–Golay Based Smoothing**:* Prior to structural analysis, the measured spectrum undergoes controlled preprocessing to suppress high-frequency measurement noise while preserving carrier envelope geometry. A Savitzky–Golay filter [11] with polynomial order $p = 3$ and window length $2M + 1 = 31$ $(M = 15)$ is applied to suppress measurement noise while preserving carrier envelope geometry and transition sharpness.

For each central bin k, the filtered amplitude $\tilde{A}(f_k)$ is obtained by solving the local least-squares problem in (2), where $c_0, c_1, \ldots, c_p$ are the polynomial regression coefficients estimated through local least-squares fitting within the sliding window, and p denotes the polynomial order of the Savitzky–Golay approximation.

$$\min_{c_0, c_1, \ldots, c_p} \sum_{i=-M}^{M} \left[A(f_{k+i}) - \sum_{m=0}^{p} c_m i^m \right]^2 \tag{2}$$

The smoothed value at the window center is given by (3).

$$\tilde{A}(f_k) = c_0 \tag{3}$$

ISBN: 978-1-68558-391-0

This formulation performs local polynomial regression rather than simple averaging, thereby suppressing random spectral fluctuations while preserving carrier peak amplitudes and transition sharpness at carrier boundaries.

The resulting smoothed spectrum $\tilde{A}(f_k)$ is subsequently used for adaptive noise floor estimation, carrier-to noise transition localization, and domain-specific interference detection. This preprocessing stage enhances the stability of threshold-based logic while retaining sensitivity to localized structural distortions within multi-carrier transponder spectra.

C. Structural Spectrum Segmentation

Prior to domain-specific analysis, the spectrum undergoes structural segmentation to establish an adaptive noise reference and to localize carrier-noise separation. These two operations define the analytical framework within which subsequent processing is performed.

Global Noise Threshold (GNT): Adaptive noise floor estimation is performed using a valley-driven sampling strategy. Local minima are identified from a smoothed representation of the spectrum using prominence-based peak detection applied to the inverted trace. For each detected valley index v_i, a neighborhood window of fixed width is sampled to collect representative noise measurements.

Let $\mathcal{N}_i$ denote the set of amplitude samples in the vicinity of the i-th valley. The GNT is defined as the median of the aggregated valley samples shown in (4):

$$GNT = \operatorname{median}\left(\bigcup_i \mathcal{N}_i\right). \tag{4}$$

The median operator provides robustness against sporadic spikes and localized interference. This threshold serves as the reference baseline for noise-domain anomaly detection.

Carrier-to-Noise Transition Localization via Hierarchical 3–7 Trend Analysis: Carrier-to-noise transition localization is performed through directed searches initiated from each carrier center toward both the left and right sides of the spectrum. The objective is to identify structurally stable transition inflection regions where carrier energy consistently decays into the surrounding noise floor. In theory, inflection points correspond to locations where the spectral slope approaches zero. However, direct gradient-based transition detection was found to be unreliable in heterogeneous transponders containing both narrow-band and wide-band carriers. Wide carriers exhibit gradual spectral slopes, resulting in weak or ambiguous first-derivative responses. To ensure robust transition localization, a hierarchical multi-point trend validation strategy is employed. The selected 3-point and 7-point trend evaluations were determined based on the acquisition resolution used throughout the experiments (5000 sweep points over a 40 MHz span, corresponding to approximately 8 kHz per sample). Empirical observation showed that these comparison lengths provided stable transition tracking across varying carrier roll-off conditions, while larger trend windows frequently extended beyond the carrier-to-noise transition region and prematurely reached the noise floor. In addition, the minimum operational carrier data rate considered during evaluation was 64 kbps. Since a 7-point observation window corresponds to approximately 56 kHz of spectral span, the trend validation remained confined within the expected transition behavior of even the narrowest operational carriers while still providing sufficient structural continuity for reliable boundary confirmation.

Initial transition qualification is triggered when the amplitude falls 2 dB below the carrier peak level, establishing a provisional containment threshold. The provisional 2 dB transition criterion was selected empirically to maintain consistency with the minimum carrier qualification condition used by the segmentation stage. Lower thresholds increased sensitivity to noise-floor fluctuations, while higher thresholds reduced boundary sensitivity for low-power carriers. Then, for each candidate index i, local monotonicity trends are evaluated using forward differences as defined in (5):

$$\Delta\tilde{A}_k = \tilde{A}(f_{i+k}) - \tilde{A}(f_{i+k-1}), \quad k = 1, 2, \ldots, N \tag{5}$$

where negative $\Delta\tilde{A}_k$ values indicate downward transitions toward the noise floor.

The detection logic proceeds as follows:

- A 3-point comparison is first applied to verify immediate downward transition consistency.
- If the 3-point validation fails, a 7-point comparison is evaluated to detect broader downward trends.
- If both checks are inconclusive, a fallback trend evaluation is performed using up to 10 consecutive points, requiring at least 75% consistency in downward slope direction.

The 75% consistency requirement was selected empirically to preserve dominant downward trend behavior without enforcing strict monotonic decay. Lower values increased sensitivity to spectral fluctuations, while higher values produced overly restrictive edge validation for closely spaced or gradual roll-off carriers. Once validated, the corresponding index is locked as the carrier-to-noise transition anchor.

D. Noise-Domain Analysis: Carrier Aware Spectral Cursor (CASC)

The Carrier Aware Spectral Cursor (CASC) operates exclusively within the noise and transition regions defined by the structural segmentation stage. Unlike global threshold detectors, CASC is explicitly aware of carrier shoulders and boundary indices derived from the 3–7 trend analysis. This awareness ensures that legitimate carrier energy is excluded from noise-domain evaluation.

1) Shoulder-Constrained Traversal

The CASC engine performs directed traversal between adjacent carriers, analyzing the spectral span from the right shoulder of one carrier to the left shoulder of the next. By confining evaluation to shoulder-to-shoulder regions, the algorithm isolates pure noise intervals while avoiding contamination from carrier interiors.

2) Noise Floor Anomaly Detection

Within each shoulder-constrained interval, instantaneous amplitude values are compared against the previously computed GNT. A noise anomaly is declared when the amplitude exceeds the adaptive threshold by a predefined margin. A 1.5 dB margin above the GNT was selected empirically to provide stable separation between normal real-time noise-floor fluctuations and significant spectral anomalies while avoiding excessive sensitivity to transient ripple variations.

Region-growing logic is applied to determine the start and end frequencies of the detected anomaly, ensuring continuous abnormal spans are grouped into a single event. Region growth is initiated when the spectral amplitude exceeds the anomaly declaration margin above the Global Noise Threshold (GNT). The detected span is then expanded across consecutive samples while the amplitude remains above the GNT and outside verified carrier regions. Growth terminates once the spectrum returns to the baseline noise regime or intersects a carrier exclusion boundary.

3) Structural Consistency Verification

In addition to noise elevation detection, CASC evaluates the structural validity of carrier-to-noise transition anchors identified by the 3–7 trend analysis. Specifically, the algorithm checks for abnormal double-rise or double-fall behavior in the vicinity of boundary indices. Such patterns may indicate falsified edge locking due to localized interference or abrupt spectral distortion.

By combining adaptive noise thresholding with transition-consistency validation, CASC provides robust detection of both distributed noise floor changes and localized transition-region anomalies.

Because carrier cores are explicitly excluded, the module remains confined to the noise domain and avoids misclassification of legitimate carrier power variations.

E. Carrier-Domain Analysis: Carrier Anomaly Detection (CAD)

Once the noise-domain assessment is completed, analysis shifts to carrier regions.

Each carrier is treated as a structured spectral entity defined by geometrically stable reference points. The carrier boundaries are determined using -2 dB transition points relative to the carrier peak. These transition points define the effective energy containment region, referred to as the Analysis Window.

All carrier-domain metrics are computed exclusively within this window.

1) Centroid Displacement

The spectral centroid is computed as a power-weighted mean frequency within the analysis window [12]. Deviation of the centroid from the geometric center provides a quantitative measure of envelope symmetry.

Centroid displacement may indicate:

- Asymmetric distortion
- Partial adjacent channel intrusion
- Compression effects

Within the analysis window bounded by f_L and f_R, let the discrete spectrum be represented as $A(f_k)$, where f_k denotes the frequency bin and $A(f_k)$ its corresponding amplitude. The power-weighted spectral centroid is computed as in (6):

$$f_c = \frac{\sum_{k=L}^{R} f_k \, A(f_k)}{\sum_{k=L}^{R} A(f_k)} \tag{6}$$

Centroid displacement relative to the geometric center f_0 is defined as in (7):

$$\Delta f = f_c - f_0 \tag{7}$$

A carrier anomaly is declared when the centroid displacement exceeds 2% of the carrier analysis-window bandwidth. This relative threshold enables consistent structural sensitivity across carriers with varying occupied bandwidths.

2) Core Deviation Metric

The observed carrier envelope is compared against a smoothed reference envelope. The aggregate deviation between the two provides a quantitative measure of distributed structural deformation within the carrier envelope.

Let $\hat{A}(f_k)$ denote the smooth envelope estimate of the carrier. The Core deviation is defined as the normalized mean absolute deviation as shown in (8) :

$$D_{core} = \frac{1}{N} \sum_{k=L}^{R} \left| A(f_k) - \hat{A}(f_k) \right| \tag{8}$$

where N = R - L + 1. This metric captures flattening, uneven shoulder behavior, and gradual envelope deformation.

3) Localized Spike Detection

Localized narrow-band anomalies within the carrier core are detected by evaluating amplitude deviations relative to the median core level. Residual excursions exceeding a predefined threshold are flagged as structural spikes. Localized spike anomalies are declared when core amplitudes exceed the median carrier-core level by 1.5 dB. This margin was selected through operational observation to reduce sensitivity to minor envelope variations while retaining detection capability for embedded narrow-band distortions. This mechanism enables detection of embedded interference components that may not significantly affect global symmetry metrics such as centroid displacement.

F. Decision Fusion Strategy

The outputs of CASC and CAD are interpreted jointly, but remain analytically independent. Decision logic distinguishes between:

- Noise-domain anomalies
- Carrier-domain structural anomalies
- Concurrent disturbances across both domains

This separation enables a clearer classification of transponder spectrum impairments and reduces ambiguity in root-cause interpretation. While CAD evaluates internal carrier structure, CASC maintains noise-domain integrity and boundary consistency, enabling reliable separation of anomaly types.

ISBN: 978-1-68558-391-0

Rather than producing a single aggregated anomaly score, the system preserves domain-level diagnostics, allowing operators to differentiate between noise elevation, carrier deformation, or combined degradation.

III. RESULTS AND DISCUSSION

This section presents the experimental validation of the proposed framework using operational satellite transponder spectra, followed by qualitative and quantitative analysis of the obtained interference detection results.

A. *Experimental Setup*

The proposed framework was evaluated using live spectrum acquisitions from multiple satellite downlinks at the ISTRAC Mission Control Center (MCC). The captured spectra reflected realistic operational loading conditions with heterogeneous carrier bandwidths and power levels. Measurements were obtained through automated acquisition using a fixed analyzer configuration to ensure repeatability. The monitored transponders contained both narrow-band and wide-band carriers operating under varying spectral occupancy conditions, enabling evaluation across heterogeneous carrier spacing and transition behaviors representative of practical FDMA-SCPC satellite deployments.

TABLE I. DATASET SUMMARY

Transponder	Frequency Band	Carrier Count
1	3965-3983 MHz	32
2	3826-3836 MHz	6
3	4550-4590 MHz	34
4	4670-4710 MHz	17

Detection robustness was assessed by introducing controlled spectral disturbances, including localized noise-floor elevation and narrow-band interference relative to known carrier positions. All experiments were performed using the implemented dual-domain architecture without manual adjustment of detected regions.

Table I summarizes the operational transponders used for evaluation, including the monitored frequency ranges and corresponding carrier counts.

For consistent interpretation, a unified visualization scheme is adopted. The GNT is shown as a horizontal grey dashed line, carrier center frequencies as vertical purple markers, and segmentation transition anchors at detected locations. Noise-domain anomalies identified by CASC are highlighted in orange, while carrier-domain anomalies detected by CAD are indicated in red.

B. *Noise-Domain Detection Performance (CASC)*

The CASC module demonstrated consistent detection of noise-floor elevation and unauthorized spectral energy within shoulder-to-shoulder noise regions. By restricting traversal strictly between carrier boundaries defined by the 3–7 segmentation stage, the algorithm avoided contamination from carrier interior energy and ensured that only noise-domain behavior was evaluated.

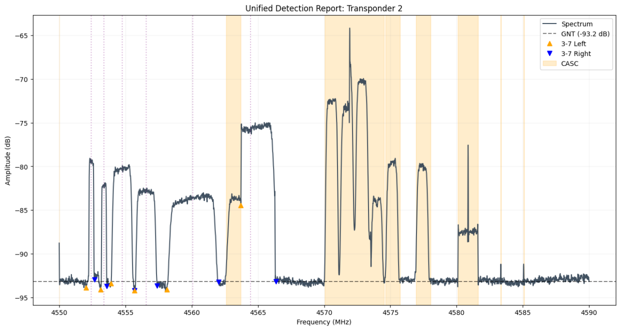

Figure 3. CASC Detection of Transition region and unaware carriers: Transponder 2

Figure 3 illustrates two distinct noise-domain detection scenarios within the same transponder spectrum. The first anomaly, observed near the left-hand side of the central carrier cluster, corresponds to a double-rise transition at a segmented carrier boundary. The boundary consistency validation stage detected this abnormal rise pattern by analyzing directional symmetry around the transition region, thereby preventing incorrect edge locking while preserving accurate carrier boundary localization.

Further toward the right of the same frequency span, multiple spectral structures appear without corresponding carrier segmentation because they are unauthorized transmissions and hence not included in the frequency plan. Since no verified carrier boundaries were established for these signals, CASC treated them as noise-domain intrusions. Using adaptive comparison against the GNT, adjacent abnormal samples were grouped into contiguous detection spans. This enabled reliable identification of previously undefined or unauthorized carriers present within the transponder bandwidth.

C. *Carrier-Domain Detection Performance (CAD)*

Within verified carrier regions, structural evaluation was performed using centroid-based symmetry analysis and core spike detection.

Centroid displacement effectively captured asymmetric carrier deformation. In cases where spectral energy distribution was skewed toward one side of the carrier bandwidth, the full-window centroid deviated measurably from the core centroid, triggering anomaly flagging. This method proved sensitive to structural leaning without reacting to uniform power scaling.

Core spike detection identified localized narrow-band distortions embedded within otherwise stable carrier envelopes. By comparing core amplitude samples against the median core level, isolated spectral spikes were reliably flagged while maintaining robustness against minor amplitude fluctuations.

Importantly, CAD processing was confined strictly to carrier-defined analysis windows, preventing noise-domain disturbances from influencing carrier structural evaluation.

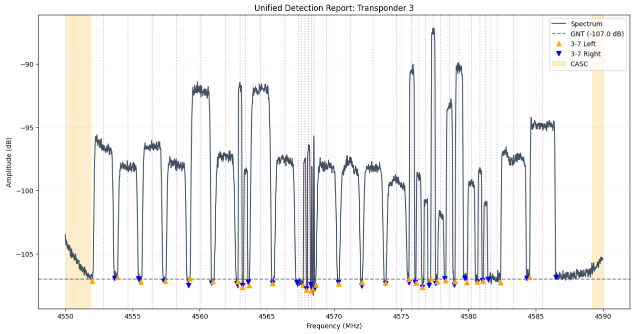

Figure 4. Unified CASC and CAD Detection: Transponder 3- Original

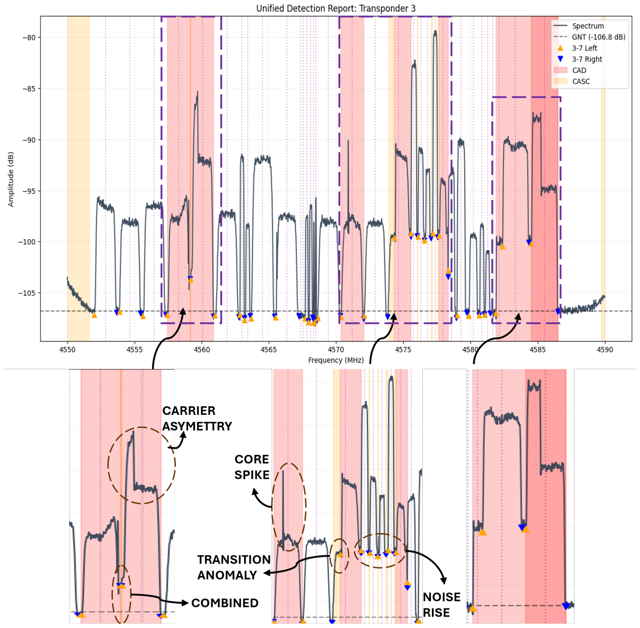

Figure 5. Unified CASC and CAD Detection Results for Transponder 3 with Multiple Injected Noise-Domain and Carrier-Domain Anomalies

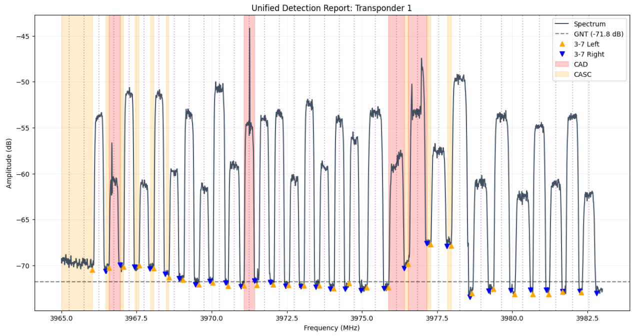

Figure 6. Unified CASC and CAD Detection Results for Transponder 1 with Multiple Noise-Domain and Carrier-Domain Anomalies, Including Nine CASC Detections and Four CAD Structural Detections

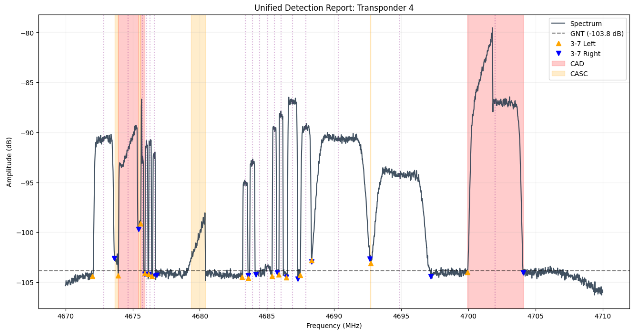

Figure 7. Unified CASC and CAD Detection Results for Transponder 4 Illustrating Unauthorized Carrier and Structural Anomaly Detection

D. *Joint Diagnostic Interpretation*

The separation of noise-domain and carrier-domain analysis provided improved interpretability compared to uniform threshold-based detection approaches. Noise floor rise events were clearly distinguished from carrier-specific structural anomalies, reducing diagnostic ambiguity.

Figure 5 illustrates the controlled interference evaluation performed on Transponder 3, where multiple representative anomaly conditions were intentionally introduced to assess both noise-domain and carrier-domain detection behavior. The highlighted regions demonstrate successful localization of unauthorized spectral activity, transition-region disturbances, carrier asymmetry, and localized structural deformation using the proposed dual-domain framework.

Table II summarizes the controlled interference scenarios evaluated during this experiment together with their corresponding detection modules and outcomes. The results confirm that CASC consistently detected noise-domain and transition-region anomalies, while CAD reliably identified structural carrier distortions and localized intra-carrier abnormalities.

TABLE II. CONTROLLED INTERFERENCE DETECTION SUMMARY

No.	Condition	Module	Result
1	Noise rise	CASC	Detected
2	Unauthorized carrier	CASC	Detected
3	Carrier asymmetry	CAD	Detected
4	Transition anomaly	CASC	Detected
5	Core spike	CAD	Detected
6	Combined distortion	CASC+CAD	Detected

In practical scenarios, this separation enabled differentiation between distributed noise elevation affecting multiple carriers and localized distortion confined to individual carriers. The resulting CAD and CASC reports provided frequency-span localization together with the corresponding anomaly rationale.

The presented results demonstrate that explicit domain separation improves reliability and interpretability in automated transponder spectrum monitoring. Figure 4 shows the nominal transponder spectrum without injected interference, while Figure 5 illustrates combined CASC and CAD detection under injected noise-domain and carrier-domain anomalies. Additional operational spectra in Figures 6 and 7 further validate consistent detection across varying transponder loading conditions, including unauthorized carrier detection by the CASC module in Figure 7.

ISBN: 978-1-68558-391-0

E. Quantitative Performance Evaluation

Quantitative evaluation was performed using known unauthorized carrier injections with predefined ground-truth (GT) frequency spans. The detected anomaly regions obtained from the proposed framework were compared against manually specified start frequency, end frequency, and bandwidth values to evaluate detection accuracy and spectral localization performance. In addition to noise-domain evaluation through CASC, carrier-domain false alarm behavior was assessed using nominal operational carriers monitored across repeated spectrum sweeps.

TABLE III. CASC NOISE-DOMAIN DETECTION PERFORMANCE

Metric	GT 1	GT 2
Start Freq. (MHz)	4626.655	4627.254
End Freq. (MHz)	4626.946	4627.546
Bandwidth	291 kHz	292 kHz
Mean IoU	0.9294	0.9285
Start Error	15.3 kHz	10.3 kHz
End Error	5.6 kHz	11.4 kHz
Bandwidth Error	3.9%	0.4%
P_d	96.1%	99.6%

The CASC module demonstrated consistent detection of unauthorized spectral activity with 96.1% and 99.6% probability of detection across all evaluated sweeps, as summarized in Table III. The high Intersection over Union (IoU) values indicate strong agreement between detected anomaly spans and ground-truth interference regions, while the low start/end frequency errors and bandwidth estimation errors confirm accurate spectral boundary localization performance.

For CAD module, evaluation was performed across nominal operational carriers to assess false alarm behavior under non-anomalous conditions. As shown in Table IV, only 22 false positive detections were observed across 3712 evaluated carriers, resulting in a false alarm probability of 0.5927%. This demonstrates that the proposed structural analysis maintains high sensitivity to carrier deformation while preserving stable operation under normal spectral conditions.

Beyond quantitative accuracy, the proposed framework demonstrated strong operational interpretability during live transponder monitoring. Because CASC and CAD preserve independent domain-level diagnostics, operators can distinguish between distributed noise-floor degradation, unauthorized spectral occupancy, and carrier-specific structural distortion without ambiguity. This separation reduces reliance on manual spectrum inspection and supports faster root-cause assessment in dense FDMA-SCPC satellite environments.

TABLE IV. CAD CARRIER-DOMAIN FALSE ALARM EVALUATION

Metric	Value
Carriers Evaluated	3712
False Positive Flags	22
True Negative Carriers	3690
False Alarm Probability (P_{fa})	0.5927%

IV. CONCLUSION AND FUTURE WORK

This work presented a structured dual-domain framework for automated monitoring of satellite transponder spectra in FDMA-SCPC environments. By introducing explicit carrier segmentation through hierarchical transition localization and adaptive noise floor estimation, the methodology establishes a deterministic structural foundation prior to anomaly evaluation. The separation of noise-domain and carrier-domain processing enables domain-specific detection without statistical cross-contamination. The Carrier-Aware Spectral Cursor (CASC) provides robust surveillance of transition and noise regions, while the Carrier Anomaly Detection (CAD) module evaluates internal carrier symmetry and localized envelope deviations. Their outputs are consolidated within a unified decision framework, preserving interpretability while improving diagnostic clarity.

Unlike uniform global thresholding approaches, the proposed architecture aligns closely with practical RF engineering reasoning and remains fully deterministic and reproducible. The framework has been successfully implemented and evaluated within the ISTRAC satellite communication environment, demonstrating practical applicability in operational multi-carrier FDMA-SCPC systems.

A. Limitations

While the proposed framework provides deterministic and interpretable spectrum monitoring, several limitations remain. Carrier segmentation currently relies on predefined carrier frequency information and fixed threshold margins, which may require retuning under significantly different transponder loading conditions. Since both CASC and CAD depend on accurate structural segmentation, boundary localization inaccuracies may propagate into subsequent domain-specific evaluations and affect anomaly interpretation. In addition, the current implementation remains threshold-driven and does not yet incorporate adaptive learning or statistical optimization mechanisms.

B. Future Work

Future work will focus on adaptive parameter optimization, enhanced structural metrics, and dynamic carrier tracking to improve robustness under highly variable spectral environments. Further development will also include full real-time deployment with integrated GUI-based monitoring for continuous operational surveillance of satellite transponders. Extending the framework toward automated interference localization and operator-assisted anomaly visualization is expected to support smoother SATCOM operations with improved reliability, detection precision, and real-time diagnostic awareness. While the present work focuses on deterministic dual-domain interference detection and operational validation within real satellite transponder environments, future investigations will include comparative performance evaluation against statistical thresholding and machine learning-based interference detection approaches using common benchmark scenarios and controlled spectral injections.

ACKNOWLEDGEMENT

The authors acknowledge Dr. A K Anilkumar, Director, ISTRAC and Shri. M R Raghavendra, Associate Director, ISTRAC for encouraging this work. Special appreciation to the SATCOM-ISTRAC team for their valuable feedback during the development and testing phases.

REFERENCES

[1] D. Roddy, *Satellite Communications*, 4th. McGraw-Hill, 2006.

[2] *ITU-R SM.1542: Methods for measurement of spectrum occupancy*, International Telecommunication Union, 2015.

[3] T. Pratt, C. Bostian, and J. Allnutt, *Satellite Communications*, 2nd. Wiley, 2003.

[4] G. Maral and M. Bousquet, *Satellite Communications Systems: Systems, Techniques and Technology*, 5th. Wiley, 2011.

[5] S. M. Kay, *Fundamentals of Statistical Signal Processing: Detection Theory*. Prentice Hall, 1998.

[6] L. Pellaco, N. Singh, and J. Jaldén, "Spectrum prediction and interference detection for satellite communications," *arXiv preprint arXiv:1912.04716*, 2019. DOI: 10.48550/arXiv.1912.04716.

[7] PyVISA Documentation, "Python visa bindings for measurement device control," 2023, [Online]. Available: https://pyvisa.readthedocs.io/ (visited on 05/2026).

[8] C. R. H. et al., "Array programming with numpy," *Nature*, vol. 585, pp. 357–362, 2020. DOI: 10.1038/s41586-020-2649-2.

[9] P. V. et al., "Scipy 1.0: Fundamental algorithms for scientific computing in python," *Nature Methods*, vol. 17, pp. 261–272, 2020. DOI: 10.1038/s41592-019-0686-2.

[10] Rohde & Schwarz, "Spectrum analyzer user manual," Manufacturer Documentation, 2022, [Online]. Available: https://www.rohde-schwarz.com/ (visited on 05/2026).

[11] A. Savitzky and M. J. E. Golay, "Smoothing and differentiation of data by simplified least squares procedures," *Analytical Chemistry*, vol. 36, no. 8, pp. 1627–1639, 1964. DOI: 10.1021/ac60214a047.

[12] A. V. Oppenheim and R. W. Schafer, *Discrete-Time Signal Processing*, 2nd. Prentice Hall, 1999.

ISBN: 978-1-68558-391-0